New Insights into the Depositional Facies of the Early Eocene Rus Formation, Bahrain

Aimen Amer, SLB, (aamer@slb.com); Pietari Skyttä, University of Turku, (pimisk@utu.fi); Antti Ojala, University of Turku, (antti.e.ojala@utu.fi); Esa Heilimo, University of Turku (esa.heilimo@utu.fi)

Abstract

Detailed geological field measurements combined with petrographic and mineralogical analyses of the Horse Racing Club outcrop, Bahrain, revealed new insights into the composition, facies distribution, and depositional settings of the Early Eocene Rus Formation, which is poorly constrained in Bahrain. The mineralogical analysis revealed that the rock-forming units are dominated by dolomite, dolomitic marl, claystone, and minor evaporites. The integration of field data and lab measurements resulted in the identification of thirteen facies that are grouped into five facies associations comprising i) lagoonal complexes, ii) sabkha complexes, iii) transgressive lag, iv) peritidal channel complexes, and v) barrier island and washover complexes. Combined paleocurrent analysis of field-observed clinoformal structures, lateral accretion surfaces, and trough cross-bedding indicate a NNW–SSE paleoshoreline trend with tidal channels trending dominantly towards NE–SW and NW–SE directions. The depositional facies model developed for the Rus Formation in Bahrain and within the surrounding region suggests that during the Early Eocene, two landmasses existed to the north and south of Bahrain, restricting the Neo-Tethys Ocean flow through a relatively narrow strait that was influenced by periodic storms. The results of this paper challenge the role of the Rus Formation as an effective regional hydrocarbon seal and, as such, highlight the need for a critical evaluation of the associated petroleum system potential in Bahrain and neighboring countries.

Key words

Facies and facies associations, integration, paleocurrent analysis, dolomite, paleogeographic reconstruction, evaporites, Neo-Tethys, storm deposits.

1-Introduction

To accumulate economic hydrocarbon reserves, the principal petroleum system elements and processes need to be in place. The elements are the source rock, reservoir, overburden, and seal, whereas the processes encompass trap formation, hydrocarbon generation, migration, and accumulation (Al-Hajeri et al., 2009). This article focuses on evaluating the Early Eocene Rus Formation, which has been widely

considered as a major seal for the Umm Er Radhuma Formation, covering large portions of the Arabian Plate (Pierce, 1993; Sharland et al., 2001).

The geology of the Arabian Plate has been, and arguably still is, an area of continued debate. For example, the United States Geological Survey (USGS) highlighted the occurrence of an oil seep in the Rus Formation in the central region of Bahrain (Willis, 1967), while the Rus Formation in Bahrain has been considered a major seal (Pierce, 1993; Sharland et al., 2001). Based on the limited published work, Sharland et al. (2001) suggested that Bahrain, alongside Saudi Arabia, Qatar, and Abu Dhabi, is dominated by evaporites.

Geological outcrop studies on Rus Formation exposures in Bahrain are scarce, and few papers have been published during the past century. In 1956, the USGS published the first geological map of Bahrain and described the exposed Rus Formation as chalky dolomitic limestones (Willis, 1967). The USGS campaign to study the surface geology of Bahrain was led by hydrocarbon exploration and the drilling of several exploration wells in the central region of Bahrain (Willis, 1967). Furthermore, drilling through the Rus Formation was characterized by drilling-mud losses, which was attributed to slumping of strata above anhydrite beds that have been leached (Willis, 1967; Fig. 1, a & b). It is believed that such an interpretation seeded the idea of the dominance of evaporites in Bahrain. Powers et al. (1966) presented the Rus Formation exposed at the Dammam Dome within the Eastern Province of Saudi Arabia as a typical soft chalky limestone dominated by evaporites with few porous beds. By contrast, Alkhalifa and Kurison (2023) described a gypsum layer of only 2.5 cm in the 56-m-thick Rus Formation exposure at the Dammam Dome, which challenges the earlier findings of Powers et al. (1966).

Despite the brief description provided by Willis (1967), the Rus Formation exposed in Bahrain has not yet been studied in detail, and neither has a representative stratigraphic column been presented. In this article, we characterize the Rus Formation exposed at the Horse Racing Club (HRC) site in Bahrain (Figs 1, c & 2) through detailed geological field descriptions, thin sections, and geochemical analyses, with the objective of deciphering its complex facies architecture and developing a representative facies model, allowing its justified usage in future hydrocarbon exploration studies.

2- Geological setting

The HRC outcrop is exposed along the northern edge of the doubly plunging Awali anticline in Bahrain, located at lat. 26° 4'20.99"N and long. 50°31'19.09"E (Figs 1 & 2). Detailed outcrop descriptions combined with the stratigraphic position of the exposure in relation to the Shark Tooth Shale Member of the

Dammam Formation (Abahussain, 2015) determined that the presently described exposed rock succession belongs to the upper Rus Formation (Figs 3 & 4). It is composed of a 26.5-m-thick section predominantly comprising dolostones and marls that correspond to the Early Eocene Rus Formation.

The formation was initially known as the "Chalky Zone", but was later renamed as the Rus Formation by Thralls and Hasson (1956). The Rus Formation is conformably underlain by the Umm Er Radhuma Formation and unconformably overlain by the Dammam Formation. The type section of the Rus Formation was introduced by Willis (1967) at the Dammam Dome (Fig. 1, a), near Jabal Umm Er Rus in Saudi Arabia (lat. 26°19'04" N long. 50°07'51" E), with a total thickness of 56 m (Weijermars, 1999). Borehole data in Bahrain indicate that the thickness of the Rus Formation can range between 125 m in the west and 73 m in the east (Zubari, 1999).

The Awali anticline initiated during the Permian, and uplifting has continued to the present day (Alsharhan and Kendall, 1986; Fig. 1, b). The mechanism behind this continuous uplifting is suggested to be the halokinesis of the underlying deep-seated Early Cambrian (Arasu and Abdulaziz, 2015) Hormuz Salt (Weijermars, 1999). The structural growth resulted in erosion over the crestal region of the anticline and was eventually responsible for the generation of prominent concentric rimrock circles in the central region of Bahrain, resulting in several distinct cliff faces (Figs 1 & 3).

The lower and middle Rus Formation units in Bahrain are represented by the Jabal al Dukhan (Mountain of Smoke) succession, which geographically represents the highest elevation point in Bahrain, at 134 m above the present-day sea level (Fig. 3). These outcrops have only been briefly studied due to access restrictions. The focus of this article is on the HRC outcrop in Bahrain, which represents the upper Rus Formation and directly underlies the Dammam Formation (Fig. 4).

3-Methodology

We conducted depositional facies analysis on the HRC outcrop in the central region of Bahrain (Fig. 1). The outcrop covers an area of 1.6 km^2 that is currently characterized by valleys, cliffs, and sand dune cover. The approach is widely used in outcrop studies under similar geological conditions (Al-Hajeri et al., 2020; Amer et al., 2019; Amrouni et al., 2016; Benham et al., 2018; Palermo et al., 2010), and comprises geological description of the outcrops supported by petrographic descriptions from thin sections, and the determination of the geochemical composition of the samples.

3.1-Outcrop characterization and sampling

The true stratigraphic thickness of the HRC outcrop units was first measured using a measuring tape. This was followed by detailed sedimentological descriptions of lithology, mineral composition, grain size, fossil content, ichnology, sedimentary structures, paleocurrent measurements, bed geometry, and lateral facies continuity to allow the construction of an accurate stratigraphic column. Based on the recognized facies changes, a total of 58 fresh rock samples representing the full diversity of sedimentary facies were acquired. For each of the field identified lithofacies, a pair of identical rock samples were selected, except for soft clay-rich units, from which thin sections could not be produced. The first set of samples (26 specimens) was allocated to thin section preparation for petrographic analyses and the second set (32 specimens) for geochemical analyses.

Outcrop field analysis also included observations and measurements of the attitudes of clinoformal structures, lateral accretion surfaces, ripples, and trough cross-bedding over the various facies to constrain the paleocurrent conditions. The dip angles of primary bedding over these outcrops were also measured in order to evaluate the structural dip (Fig. 3).

3.2-Petrographic analysis

Petrographic analysis included the determination of porosity and a basic petrographic description (e.g., mineralogy, alteration, grain size and shape, fabric) of the samples from thin sections and elemental analysis. Twenty-six samples were prepared by SLB Dhahran Carbonate Research lab in Saudi Arabia for thin-section preparation.

A digital thin section image analysis method (Astuti et al., 2018) was implemented to calculate porosity values using a 30 mm^3 full-color thin-section micrograph. The micrograph image was first processed to a gray-monochrome pixelated image that separated the image into two parts, namely the rock and total area. A threshold was then applied to the color spectrum to be able to identify the areas with blue epoxy, which are considered to represent pore spaces. This threshold was later used to quantify the porosity percentages.

3.3-Geochemical analysis

X-ray diffraction (XRD) analysis was performed to determine the mineral amounts of the collected samples. XRD analyses were executed by the CRE SLB Geoservices Mud Logging lab using the bulk powder approach, in which 5 g of the rock is mixed with 10 mL of isopropanol, followed by milling for 5 minutes in a McCrone Mill. The resulting suspension was rinsed from the grinding jar and dried in an oven at 70 °C for 8 hours. The samples were then packed into a sample tray and analyzed with a Bruker D8 Advance X-

ray diffractometer from 5° to 70° 2θ with a fixed rate of 1° per minute and a step size of 0.02°2θ (Zhang et al., 2005; Appendix A). The XRD mineral amounts are described within the facies descriptions.

X-ray fluorescence (XRF) analysis was also carried out in the CRE SLB Geoservices Mud Logging lab to determine the major and some trace element concentrations from whole rock samples. The powder analysis method was used, in which samples are milled and dried at 105 °C for 8 hours. Four grams of each sample was weighed and placed into a TrimLess Sleeved sample cup (Chemplex Industries, Inc.) fitted with a Prolene film (Chemplex Industries, Inc.) (Pearson et al., 2018). Samples were then analyzed using a Rigaku NEX CG Energy-Dispersive X-ray fluorescence spectrometer (Sabri, 2020; Appendix A).

4-Results

4.1-Facies description

The following section presents the facies description results as gained through the integration of outcrop and petrographic analyses (Fig. 5). Altogether, thirteen facies were defined and grouped into five facies associations, which are described in the following sections (Table 1).

4.1.1- Facies association 1 (FA-1)

Facies association FA-1 is composed of four lithofacies (Table 1): chalky dolostone (F1), lithoclastic chalky dolostone (F2), peloidal dolostone (F3), and foraminiferal dolostone facies (F4).

4.1.1.1- Chalky dolostone facies (F1)

The F1 facies is white, dolomudstone to wackestone in texture, containing scattered calcite geodes, and is characterized by clotted micrites associated with a peloidal fabric. XRD analysis indicates that the facies is composed of 100% dolomite (Appendix A), and the porosity is characterized by interparticle pores ranging from 4 to 8%. Foraminifera appear to be absent, and the facies is associated with dark brown to black hematite spots that have most likely resulted from pyrite oxidation (Figs 6, a & 7, a). Bioturbation is common and dominated by *Thalassinoides* burrows, whereas bedding is generally poor, but can be well developed in parts. Syndepositional faults dominantly reflecting normal and less frequent reverse displacement occur in places within this facies (Fig. 8).

4.1.1.2- Lithoclastic chalky dolostone facies (F2)

The F2 facies is white to gray, dolomudstone to floatstone in texture, with angular micrite rip-ups that are associated with large (>6 mm) angular clasts embedded in micritic sediments (Fig. 6, b). Based on XRD

analysis, this facies is composed of 89% dolomite, 6% calcite, 2.5% quartz, and 2.5% siderite (Appendix A). Dark brown to black hematite spots are sparsely distributed (Fig. 6, b), and the lower contact of this facies is characterized by an irregular wavy surface. The clasts observed in the F2 facies are formed by dissolved foraminifera shell aggregates that form secondary moldic pores, which can reach up to 10% (Table 1).

4.1.1.3- Peloidal dolostone facies (F3)

The F3 facies is characterized by an off-white to yellow color with a packstone texture, is well bedded, and contains occasional clotted micrites, common peloidal fabric, occasional oscillation ripples, and scouring features in some locations (Fig. 7, a). XRD analysis indicates that this facies is composed of 96% dolomite and 4% quartz (Appendix A). Leached foraminifera are observed, and bioturbation is a common feature in the lower part of the unit, which is dominated by *Thalassinoides* burrows. The studied facies is dominated by intergranular and leached porosity, which is measured at 11% (Fig. 6, c).

4.1.1.3- Foraminiferal dolostone facies (F4)

The F4 facies is ivory to off-white, comprising dolostones with a mudstone to floatstone texture, calcite geodes, *in situ* bivalve shells, gastropod molds, and shell fragments. Chert nodules are common towards the top of the sequence (Fig. 7, c), with dispersed to loosely packed foraminifera (Fig. 7, d–f). The foraminifera are dominated by *Alveolina*, while *Nummulites* are less common (Figs 6, d–f & 9, a). Framboidal pyrite is observed to occur inside foraminifera shells and in some cases can be found rimming the outer shells (Figs 6, f & 9, a). This facies is associated with fossilized mangrove trees (Fig. 10, a & b), where the trunks and root systems (*Rhizoliths*) can be well preserved (Fig. 9, b & e). XRD analysis indicates that this facies is composed of 77% dolomite, 18% illite, and 5% pyrite (Appendix A). This facies is poorly bedded to massive and water escape structures are commonly observed from the outcrops (Fig. 10, c). The porosity is 3% and is dominated by the dissolution of preexisting constituents (moldic type).

4.1.2- Facies association 2 (FA-2)

Facies association FA-2 is composed of two lithofacies: the claystone (F5) and evaporite facies (F6) (Table 1).

4.1.2.1- Claystone facies (F5)

The F5 facies is characterized by buff to green-yellowish, soft to elastic, oxidized red laminae and highly deformed clays and marls. This facies is commonly associated with extensive syndepositional deformation, brecciated fragments, and dolomitic beds of F2 and F9 facies that contain injectites (Fig. 11,

a). Few layers exhibit a high concentration of halite that is associated with desiccation cracks, and quartz pseudomorphs after gypsum of the F6 facies can be associated with this facies (Fig. 11, b & c). XRD analysis indicates that this facies is composed of 100% illite (Appendix A).

4.1.2.2- Evaporite facies (F6)

Typical for this facies are brown *in situ* vertically elongated crystals, which are mainly composed of quartz pseudomorphs after gypsum, with XRD analysis indicating that the crystals are composed of 57% quartz and 43% dolomite (Appendix A). This facies is associated with thin laminae of rare halite and desert rose quartz pseudomorphs after gypsum. The facies is characterized by a limited occurrence, with the lateral extent rarely exceeding 30 m and thicknesses not exceeding 50 cm (Fig. 11, d & e).

4.1.3- Facies association 3 (FA-3)

Facies association FA-3 is composed of two lithofacies: the argillaceous dolostone (F7) and foraminiferal dolostone facies (F4) (Table 1).

4.1.3.1- Argillaceous dolostone facies (F7)

The characteristic features of this facies include a white to ivory color, very hard, packstone texture with clotted micrite fabric, abundant leached foraminifera, and subangular lithoclasts (Fig. 9, d). XRD analysis indicates dolomite-dominated mineralogy (82% dolomite and 18% illite) (Appendix A). This facies is laterally continuous, poorly bedded to massive, and associated with an erosional basal contact marked by lag deposits. Bioturbation is common and dominated by *Ophiomorpha* burrows (Fig. 11, f & g). The porosity is characterized by the interparticle and moldic type and is measured at 7% (Table 1).

4.1.4- Facies association 4 (FA-4)

Facies association FA-4 is composed of four lithofacies (Table 1): the dolomitic marl (F8), bioturbated chalky dolostone (F9), cross-bedded dolostone (F10), and microbial dolostone facies (F11).

4.1.4.1- Dolomitic marl facies (F8)

Typical for this facies is yellowish green to reddish, soft to friable sediments with a mudstone texture, although towards the top of this facies they can be hard and associated with mangrove roots (Fig. 9, e & f). The facies is dominated by marls to argillaceous dolostone that can have a thinly laminated appearance. Clinoformal structures that are marked by red laminae, imbrication structures, and dip towards the SE direction are also observed (Fig. 12, a). This dolomitic marly facies can contains fossil-rich beds (subfacies)

that are rare and only observed towards the base in a few localities. The fossil assemblages comprise bivalves, shell fragments, and *Nummulites* (Fig. 12, b–d). XRD analysis indicates that the composition is 75% dolomite and 25% illite (Appendix A).

4.1.4.2- Bioturbated chalky dolostone facies (F9)

This facies is characterized by off-white to yellow chalky dolostones with a peloidal wackestone to packstone texture, is well bedded to massive, and characterized by dissolved foraminifera fragments (Fig. 13, a). The basal contact is erosional and marked by lag deposits (Fig. 12, e). Bioturbation is common at the base, with *Thalassinoides* burrows and large-diameter steeply inclined burrows that curve at the base being observed (Fig. 12, f & g). XRD analysis indicates that this facies is composed of 98% dolomite and 2% quartz, and moldic porosity being measured at 12% (Appendix A; Table 1).

4.1.4.3- Cross-bedded dolostone facies (F10)

The characteristic features of this facies include ivory to cream dolostones with a grain supported texture (grainstone) and trough cross-bedding. Grains are moderately sorted and are composed of foraminifera, echinoderm spines, shell fragments, concentric ooids, fecal pellets, and quartz grains (Fig. 13, b–e), where in some cases grains can be extensively leached (Fig. 13, f). Grainstone lenses that are characterized by flat tops and irregular bases, resembling channels, are common in this facies. Bioturbation is dominated by *Ophiomorpha* burrows that can be filled by overlaying material, whereas intense bioturbation can lead to a massive appearance (Fig. 12, h & i). XRD analysis was performed on one sample that revealed extensive leaching and indicated that the composition is 100% dolomite (Appendix A). Thin section analysis was performed on two samples collected from two different areas within the study area. One displayed extensive selective leaching, whereas the second showed less leaching. Thin section mineralogical analysis performed over the latter indicated that the rock is composed of 88% dolomite and 12% detrital quartz. Porosity is represented by intergranular and leached porosity and is measured at 17% (Table 1). Paleocurrent measurements of the various cross-beds observed over several individual lens-shaped channel bodies indicate a dominant WNW dip trend, while opposing SE directional dips are also present, but are a minority (Fig. 14, a & b).

4.1.4.4- Microbial dolostone facies (F11)

This facies is characterized by bright white to gray, buff wavy microbial laminae (on average 0.25 mm) (Fig. 14, c & d), wackestone to floatstone, fenestral porosity, peloidal fabric, clotted micrite, rare bioturbation, abundant foraminifera, Ostracoda carapace shells, and shell fragments (Fig. 15, a–c). The

foraminifera are identified as *Miliolids and Alveolina* (Fig. 15, c–e). Brecciated peloidal lithoclasts are common towards the base (Fig. 15, f) and are associated with Thrombolites, whereas the upper part is more stromatolitic (Fig. 14, d). XRD analysis revealed a predominantly dolomite composition (91%) and moderate amounts of detrital quartz (9%) (Appendix A). On average, porosity is measured at 9% and is represented by fenestral and leached porosity (Table 1).

4.1.5- Facies association 5 (FA-5)

Facies association FA-5 is composed of two lithofacies (Table 1): the bedded dolostone (F12) and clinoformal dolostone facies (F12).

4.1.5.1- Bedded dolostone facies (F12)

This facies is characterized by a buff to white color, is well bedded, and composed of dolostones with a wackestone to packstone texture, medium- to fine-grained lithoclasts and detrital quartz grains that are observed as lag deposits, rare dark brown to black hematite spots, peloids, and unidentified leached foraminifera shells fragments (Figs 14, e & 15, g). The lower contact of this facies is erosional and reflects extensive syndepostional deformation (i.e., microfaults, pillow and flame structures) (Fig. 16, a). XRD analysis indicates that the sample is 100% dolomite (Appendix A). The porosity is measured as 15% and is dominated by leached porosity (Table 1).

4.1.5.2- Clinoformal dolostone facies (F13)

The characteristic features of this facies include a gray to yellow color, mudstone to wackestone texture, occasional bivalve molds, water escape structures, and very fine to medium subangular to subrounded detrital sand grains (Fig. 14, e & f). This facies is well bedded and associated with large-scale cross-bedding that resembles clinoformal structures (Fig. 16, a–d). This unit also exhibits common syndepostional microfaults, as well as calcite geodes (Fig. 16, a). Detailed analysis of the clinoforms indicates that they are linked to ridges that appear on the top surface of this layer, which are associated with *Thalassinoides* burrows and predominantly dip towards WSW (Fig. 16, c & d). XRD analysis indicates that the sample is 89% dolomite and 11% quartz (Appendix A). The porosity is measured as 5% and is dominated by intergranular porosity (Table 1).

4.2- Geochemical analysis

The XRD analysis performed on 32 samples from the HRC study area of the Rus Formation indicates that 88% of the samples are predominantly composed of dolomite, with minor associated minerals such as

quartz, calcite, and illite (Appendix A). The relationships between several major and trace elements have been analyzed using the XRF method, and the results indicate a dominant positive correlation between selected elements. Ca/Mg, Si/Al, Al/Fe, Ti/Zr, Ti/Al, K/Rb, and K/Ba correlate positively, whereas Si/Ca correlate negatively (Fig. 17).

5-Discussion

Over the past decades, the Rus Formation in Bahrain has largely been considered as a hydrocarbon seal (Pierce, 1993; Sharland et al., 2001), although no hydrocarbon discovery has been attributed to the Rus seal. By contrast, Bahrain is known to have freshwater springs (Madany and Akhter, 1990), and oil seeps have been documented at Rus Formation exposures (Willis, 1967), suggesting that this formation is not an effective seal. These equivocal observations derive from the limited literature that describes the Rus Formation facies and depositional settings in Bahrain, which are revealed and discussed in the following sections (Fig. 5).

5.1-Facies and facies associations

5.1.1- Facies association FA-1

We interpret facies association FA-1 as a lagoon complex that has been intermittently subjected to storm events. The chalky dolostone facies (F1) of FA-1 demonstrates the absence of foraminifera, which could suggest a stressed and restricted environment (Gaaloul et al., 2022). This understanding is supported by the presence of hematitic spots, which most likely formed through the oxidation of pyrites (Wignall et al., 2005). The presence of peloids indicates bioactivity along with bioturbation over some zones and areas across the exposure, which suggests periodic episodes of restricted marine incursion. Based on these observations we postulate that the F1 facies has been deposited in a stressed lagoon setting.

The lithoclastic chalky dolostone facies (F2) of FA-1 displays a unique combination of fine micritic dolomudstones that imply a low-energy setting and angular coarser clasts suggesting episodes of high energy (Donato et al., 2009). The clasts are dominated by dissolved foraminifera shells, suggesting erosion and short-distance transportation from the lagoon outer rim (Tucker and Jones, 2023). This facies is only found embedded in the F1 facies and shares the observation of hematitic spots. These observations, in addition to the thin nature of these beds (Fig. 9), suggest that these beds have been deposited during a storm event(s).

The peloidal dolostone facies (F3) of FA-1 overlays the F1 facies, suggesting that this facies is part of the lagoonal system. However, they are predominately overlain by sabkha clay-rich facies (Fig 7, a), which suggests a change in the depositional setting. The presence of scouring, lithoclasts, bioturbation, and a small amount of detrital quartz indicates a shallow setting, which most likely corresponds to a lagoonal fill and shallowing water depth setting, marking the final lagoonal fill deposits (Biguenet et al., 2023).

The presence of foraminifera in the foraminiferal dolostone facies (F4) of FA-1, such as *Alveolina* (Figs 6, e & 7, d), suggests a restricted lagoonal depositional environment (Sarkar and Das, 2022). Such an interpretation is supported by the presence of fossilized mangrove forests, which indicate a shallow marine protected setting (Palit et al., 2022).

The F1, F2, and F3 facies of the FA-1 facies association have measured porosities of 6%, 10%, and 11%, respectively. Based on a global reservoir database of 581 producing zones of oil and gas fields, Ehrenberg et al. (2009) concluded that the porosity of Paleogene carbonate reservoirs ranges on average between 5% and 20%, making the F1, F2, and F3 facies potentially good reservoirs.

5.1.2- Facies association FA-2

We interpret facies association FA-2 as a sabkha complex predominantly composed of claystone facies (F5). The clay content of this facies suggests a low energy environment and the oxidized laminae suggest subareal exposure. The presence of halite, desiccation cracks, and quartz pseudomorphs after gypsum (Fig. 11, a-c) indicates that this facies deposited in an arid environment proximal to the shoreline, suggesting a sabkha depositional setting (Walker, 2006). The second facies of FA-2 is the evaporite facies (F6). The *in situ* nature of the vertically elongated crystal growth (Fig. 11, d & e) suggests that the gypsum growth initiated in a supersaturated brine solution. Such a setting is generally associated with a salina setting (Carlson, 1987; Kendall, 1978). This interpretation is supported by the limited lateral extent of the F6 facies (Fig. 11, e), suggesting that the salina represented a small fraction of a larger sabkha depositional environment.

5.1.3- Facies association FA-3

Facies association FA-3 is composed of the argillaceous dolostone facies (F7) and foraminiferal dolostone facies (F4). The erosive basal contact associated with lag deposits of the F7 facies suggest a high energy environment (Fig. 11, f). The argillaceous content of this facies is most likely a result of sediment reworking, as indicated by the subangular lithoclasts (Fig. 9, d), and the massive to poorly bedded nature

could suggest sediment dumping, a fast rate of sedimentation, and intensive bioturbation (Droser and Bottjer, 1986). The *Ophiomorpha* burrows indicate a marine setting (Fig. 11, g), which would suggest marine transgression, especially when found overlaying inland facies (Ryer and Anderson, 2004). Based on these observations, combined with the relatively thin thickness, we postulate that this facies represents a transgression lag.

The F7 and F4 facies of the FA-3 facies association have measured porosities of 7% and 3%, respectively. Based on the global average porosity for Paleogene carbonate reservoirs (Ehrenberg et al., 2009), only the F7 facies may be considered as a potential reservoir. However, due to its relatively thin nature, this facies may not support a reservoir with economic volumes, unless it is connected to or juxtaposed against other reservoir facies.

5.1.4- Facies association FA-4

Facies association FA-4 is comprised of dolomitic marl (F8), bioturbated chalky dolostone (F9), cross-bedded dolostone (F10), and microbial dolostone facies (F11). Based on this, we postulate that this facies association represents a peritidal complex.

The F8 facies is typically associated with lagoonal settings (Nasiri et al., 2019) because of the high amount of dolomud between the grains, indicating a low-energy and calm environment (Fürsich et al., 2003). Although such an interpretation is plausible, the presence of fossil fragments (Fig. 12, b & c) suggests sediment reworking, which requires a high-energy environment, such as storms (Donato et al., 2009). The clinoformal structures marked by red laminae resemble lateral accretion surfaces, which reflect point-bar migration (Díez-Canseco et al., 2014), suggesting the growth of a meander bend over the F8 facies (Fig. 12, a). The high content of clay over point bars is common in blind tidal channels (Ghinassi et al., 2021), and consequently we consider this facies to have been deposited in an intertidal flat setting. The SE paleocurrent direction in a such case (Fig. 5) reflects the bar migration direction, indicating a NE–SW channel axis.

The flat top and erosional base lenticular bedform of the F9 facies resembles a channel geometry (Fig. 12, e). The intensive bioturbation, with the associated peloidal fabric and foraminifera, indicates a marine influence (Tucker, 1985). The absence of clearly observed cross-bedding and the variation in the burrow sizes may suggest a protected inland setting with relatively lower or fluctuating energy, which is expected in a restricted setting (Weimer et al., 1982). Therefore, it is postulated that the F9 facies represents an inland tidal channel.

The trough cross-bedding grainstone bed forms of the F10 facies most likely occurred in relatively deeper waters with high energy (Mullins and Neumann, 1979). This is supported by the *Ophiomorpha* burrows and the concentric ooidal grains, which suggest a submarine setting (Shinn, 1983) in an agitating environment (Davies et al., 1978). Based on these observations, combined with the faunal content of foraminifera, shell fragments, fecal pallets, and echinoid spines, in addition to the stratigraphic position of these bedform, we postulate that this facies represents a tidal channel inlet setting. The paleocurrent data measured over two inlet channel systems indicate a WNW and SE paleoflow direction (Fig. 5). The combination of the two channel measurements indicates a general WNW–ESE and NW–SE tidal channel orientation.

Over the studied stratigraphic section, three microbial intervals characterized by the F11 facies are recognized (Fig. 5). The presence of laminated stromatolites suggests a subtidal setting, whereas thrombolites favor an intertidal setting (Hickson and Lamb, 2012; Reid et al., 2012, 2011). The base of the microbial layers is associated with brecciated peloidal lithoclasts (Fig. 15, f), and they are dominated by thrombolitic clusters (Fig. 14, d). This suggests that the lower portion of the F11 facies is dominated by intertidal shallower waters, characterized by relatively higher energy, whereas towards the upper part of the facies, a deeper subtidal setting was more dominant (Jahnert and Collins, 2013). The presence of microbialites in associates with abundant foraminifera, , such as *Alveolina*, indicates that this facies was most likely deposited in a subtidal to intertidal setting within a restricted lagoon.

The facies association FA-4 is considered to have the highest reservoir potential, with F9, F10, and F11 having porosities of 11%, 17%, and 9%, respectively. The F10 facies has by far the best reservoir quality in the study area, making it an excellent reservoir or groundwater aquifer (Zubari, 1999; Zubari and Khater, 1995), based on the Paleogene carbonate reservoirs around the globe (Ehrenberg et al., 2009).

5.1.5- Facies association FA-5

Facies association FA5 is comprised of bedded dolostone (F12) and clinoformal dolostone facies (F13), reflecting a barrier island and washover depositional environment.

The F12 facies is genetically associated with the F13 facies, representing the basal unit of this facies association. The erosional lower contact of the F12 facies is marked by lithoclasts and sub-rounded medium to fine sand grains, in addition to large-scale soft sediment deformation and syndepostional faulting (Figs 14, e–f & 16 a–b). The sands in this carbonate-dominated environment suggest an aeolian origin, whereas the lithoclasts indicate a high energy event. We suggest that the erosional base developed

during a storm event associated with a sandstorm, accounting for the sand grains and lithoclasts (Boggs, 2009). We further postulate that wind and wave activity resulting from a storm event moved large amounts of sediments, forming a spit sand bar system that eventually evolved into a barrier island (Reinson, 1984). The bedding planes of this facies towards the top suggest a protected setting, and we therefore consider that the F12 facies represents a back barrier facies.

The bedform geometry associated with the F13 facies suggests that deposition took place over an inclined surface, which is responsible for the formation of clinoforms and ridges (Fig. 16, b–d). The dominance of large-scale soft sediment deformation and dewatering structures is most likely a product of high deposition rates (Amer et al., 2019). Based on the stratigraphic position and bedform geometry, we attribute this facies to a washover barrier island setting (Rodriguez et al., 2018). Paleocurrent measurements of the clinoforms and ridges suggest a NNW–SSE-striking paleoshoreline.

The F12 and F13 facies of the FA-5 facies association have porosities of 15% and 10%, respectively, making the F12 facies the second-best reservoir facies in the HRC study area. Such porosity ranges are considered to be very good (Ehrenberg et al., 2009), and rather than being dominated by an evaporitic sequence with only a few porous beds (Powers et al., 1966), the Rus Formation in Bahrain is dominated by dolomites, and nine out of the thirteen facies identified have porosity values in the range of global Paleogene carbonate reservoirs.

5.2- Geochemical and mineralogical analysis

Relationships between some of the elements from the Rus Formation in Bahrain are visualized in Figure 17. The distribution of calcium is clearly opposite to that of silica (Fig. 17, a). Silica is likely to represent mineral components, especially quartz sourced by wind, while calcite is mainly derived from carbonate minerals. Calcite over the study area is positively correlated with magnesium (Fig. 17, b). The relationship suggests that carbonate minerals are the sole carrier of magnesium in the samples. In the studied carbonate samples, the Mg/Ca ratio ranges from 0.17 to 0.64 (Appendix A). This indicates that the progression of dolomitization has resulted in the dominant carbonate minerals (Krajewski et al., 2001). The relationship between silica and aluminum suggests that these elements are strongly correlated in the studied samples (Fig. 17, c), which reflects the occurrence of Si in both silicate (e.g., clays) and free silica modes (e.g., detrital) (Shaltami et al., 2020). During weathering, ferric iron and aluminum accumulate relative to one another because of the extreme insolubility of their oxides and hydroxides (Macquaker et al., 1997). In the present study, iron is strongly correlated with aluminum (Fig. 17, d), and we suggest that

most of the iron is sourced by the aluminum silicates (e.g., illite). The strong positive correlation between titanium and aluminum suggests that titanium is also contained in aluminum silicates (Fig. 17, f). Titanium and zircon are considered immobile compared to other elements during various weathering processes, inferring the terrigenous provenance (McLennan et al., 1993). The positive correlation suggests a sorting control on terrestrial sediment transportation (Fig. 17, e).

The XRD analysis revealed that the rock-forming units are mostly represented by dolomite, apart from claystone, in which they are predominantly composed of illite and evaporites, which are represented by quartz pseudomorphs after gypsum (Table 1; Appendix A). The siliciclastic content found within the F2, F3, F11, and F13 facies is of interest, because they are carbonate-dominated facies with minor amounts of sand grains (Fig. 14, f). Combined with the knowledge that storms did play a role in developing a few facies over the study area (F2 and F13), it is postulated that the very fine, fine, and medium sand grains were transported to the study area through sandstorms from the nearest landmasses during the Early Eocene. Similar sand grain size distribution patterns are observed in ancient and modern sand storm deposits of the Tengger Desert, China, where sand grains have been transported approximately 1000 km from the source area (Qingyu et al., 2010). Furthermore, the geochemical analysis performed over the HRC exposure suggests that the terrestrial source could be related to the Arabian Shield, because of similarities in compositional fractions, in particular the zirconium-titanium percentages, which are found to be diagnostic of the Arabian Shield (Quick and Bosch, 1990).

5.3-Facies model

The facies associations indicate that the depositional environment of the HRC outcrop site in Bahrain is represented by a lagoon setting that is restricted by a barrier island associated with tidal channels and sabkhas (Figs 18 & 19). Furthermore, the system is affected by relative sea level fluctuations and changes in weather patterns, resulting in transgressive lag and storm deposits. Paleocurrent data obtained from the tidal channel inlets exhibit a bimodal dip pattern that indicates a WNW–ESE paleoflow direction with minor dispersion (Fig. 5). The lateral accretion surfaces observed over the dolomitic marl facies suggest a NE–SW inland tidal channel paleoflow direction, whereas the clinoformal beach ridges indicate an approximately orthogonal NNW–SSE barrier island axis (Fig. 18).

Integrating the local observations from this work in Bahrain with subsurface data from 254 wells that penetrate the Rus Formation in Bahrain (Zubari, 1999), outcrop observations over the Dammam Dome in Saudi Arabia, Eastern Province (Weijermars, 1999), and Qatar surface and subsurface data (Al-

Hajari and Kendall, 1992), we reconstructed the paleogeography of the region (Fig. 19). The reconstructed paleogeography indicates that during the Early Eocene, two landmasses existed to the north and south of Bahrain that restricted the flow of the Neo-Tethys Ocean.

6- Conclusions

This investigation demonstrated that the debated Early Eocene Rus Formation facies is not evaporitic in composition in Bahrain. Detailed geological analysis of the HRC outcrop indicates that the exposed carbonate units are dominated by dolomites, which are interbedded with minor clay and marl units. We identified thirteen facies within the study area and further grouped them into five facies associations (FA-1 to FA-5). The recognized facies include chalky dolostone (F1), lithoclastic chalky dolostone (F2), peloidal dolostone (F3), foraminiferal dolostone (F4), claystone (F5), evaporite (F6), argillaceous dolostone (F7), dolomitic marl (F8), bioturbated chalky dolostone (F9), cross-bedded dolostone (F10), microbial dolostone (F11), bedded dolostone (F12), and clinoformal dolostone facies (F13). These facies predominantly have good porosity, reaching up to 17%, except for F5 and F6, giving the Rus Formation a high potential for being a good reservoir in Bahrain, contrary to previous assumptions.

The interpreted facies associations reflect a lagoonal system that is restricted by a NNW–SSE-trending barrier island and washover complex as a result of episodic storms, supplying detrital sand grains from the Arabian Shield. Towards the inland part of the lagoon, a sabkha environment was developed, and this environment is associated with NE–SW and NW–SE-trending tidal channel systems and small salina evaporitic puddles. This system recorded marine transgression events as transgressive lag deposits that reworked the laterally extensive carbonate and clay material overlying F8 and F11 facies, before retreating and giving way to a second cycle of sedimentation. The integration of data collected from neighboring counties revealed that two landmasses were present during the deposition of the Rus Formation in Bahrain. The first landmass was located in the northern region of Bahrain, whereas the second was to the south of Qatar, leading to the development of a NE–SW strait of the Neo-Tethys Ocean during the Early Eocene.

This study revealed that the Rus Formation can no longer be considered a major seal in the region because of the very limited extent and thickness of the evaporitic facies and the dominance of porous rocks. Extending such work across the Arabian Peninsula with a focus on the Rus Formation would potentially identify areas with significant evaporitic facies, and hence also a higher potential for the presence of a regional hydrocarbon seal.

7- Acknowledgements

We would like to thank Dr Wael Abdallah from SLB Dhahran Carbon Research (SDCR) for sponsoring the thin section and elemental analysis. We thank Ahmad AlZoukani and Vijaya Puvvala for preparing and photographing the thin sections. The authors would also like to thank Wadhah Haithm and Abdulaziz Alanazi for performing the elemental analysis at the CRE SLB Geoservices Mud Logging lab. In addition, would like to extend our deepest gratitude to Dr Khaled Amrouni from Texas A&M for his productive discussions during the field work and Prof Ahmed Muftah from the University of Benghazi for his support in the foraminifera interpretation.

8- References

Abahussain, A.A., 2015. THE MINERALOGY, GEOCHEMISTRY AND SEDIMENTATION OF THE SHARK TOOTH SHALE MEMBER, BAHRAIN. Iraqi Bulletin of Geology and Mining 11, 45–58.

Al-Hajari, S.A., Kendall, C.G.S.C., 1992. The sedimentology of the Lower Eocene Rus Formation. J. Univ. Kuwait (Sci.) 153–172.

Al-Hajeri, M., Amer, A., Green, D., Djanawair, D., Naqi, M., 2020. Origin of enigmatic sand injectite outcrops associated with non-tectonic forced-folding structure in Bahrah area, northern Kuwait Bay.

Al-Hajeri, M.M., Al Saeed, M., Derks, J., Fuchs, T., Hantschel, T., Kauerauf, A., Neumaier, M., Schenk, O., Swientek, O., Tessen, N., 2009. Basin and petroleum system modeling. Oilfield Review 21, 14–29.

Alkhalifa, M.A., Kurison, C., 2023. Karst collapse and gypsum-filled veins in Eocene outcrops, Dammam Dome, Saudi Arabia: Causes and implications. Geosystems and Geoenvironment 2, 100109. https://doi.org/10.1016/j.geogeo.2022.100109

Alsharhan, A.S., Kendall, C.G.S.C., 1986. Precambrian to Jurassic rocks of Arabian Gulf and adjacent areas: their facies, depositional setting, and hydrocarbon habitat. AAPG bulletin 70, 977–1002.

Amer, A., Al-Hajeri, M., Najem, A., Al-Qattan, F., 2019. Facies architecture of Lower Fars Formation at Jal Az-Zor escarpment, Kuwait. Arab J Geosci 12, 502. https://doi.org/10.1007/s12517-019-4622-7

Amrouni, K., Pope, M., El-Hawat, A., Obeidi, A., Amer, A., Elbargathi, H., El-Gahmi, M., Al-Alwani, A., Elbileikia, E., Mustafa, K., 2016. Palaeoshoreline and Prograding Clinoforms of Oolitic Grainstones of the Miocene Carbonate-Evaporitic Sequences of the Ar-Rajmah Group, Al-Jabal Al-Khdar Uplift and Soluq Trough, Cyrenaica, NE Libya.

Arasu, R.T., Abdulaziz, A.S.H., 2015. Sub-circular seismic anomalies of the Triassic-Paleozoic sequences and their probable linkage to deep-seated Hormuz salt pillows in Umm Gudair area, south Kuwait, in: 2015 SEG Annual Meeting. OnePetro.

Astuti, N.H., Wibowo, N.A., Ayub, M.R.S.S.N., 2018. The Porosity Calculation of Various Types of Paper Using Image Analysis. JPFI 14, 46–51. https://doi.org/10.15294/jpfi.v14i1.9878

Benham, P., Cheers, M.J., Freeman, M., Choudhary, P., Tanoli, S., Warrlich, G., Capello, M., Al-Rabah, A.A., 2018. From Outcrop to Producing Reservoirs: Applying Jal Az Zor Outcrop Studies to A Multi-Disciplinary Development Approach In Kuwait Heavy Oil Fields. Presented at the SPE International Heavy Oil Conference and Exhibition, Society of Petroleum Engineers. https://doi.org/10.2118/193686-MS

Biguenet, M., Chaumillon, E., Sabatier, P., Bastien, A., Geba, E., Arnaud, F., Coulombier, T., Feuillet, N., 2023. Hurricane Irma: an unprecedented event over the last 3700 years? Geomorphological changes and sedimentological record in Codrington Lagoon, Barbuda. Natural Hazards and Earth System Sciences Discussions 1–41.

Boggs, S., 2009. Petrology of sedimentary rocks. Cambridge university press.

Brown, G.F., Schmidt, D.L., Huffman Jr., A.C., 1989. Geology of the Arabian Peninsula; shield area of western Saudi Arabia (USGS Numbered Series No. 560- A), Geology of the Arabian Peninsula; shield area of western Saudi Arabia, Professional Paper. U.S. Geological Survey, Reston, VA. https://doi.org/10.3133/pp560A

Carlson, E.H., 1987. Celestite replacements of evaporites in the Salina Group. Sedimentary Geology 54, 93–112.

Davies, P.J., Bubela, B., Ferguson, J., 1978. The formation of ooids. Sedimentology 25, 703–730. https://doi.org/10.1111/j.1365-3091.1978.tb00326.x

Díez-Canseco, D., Arz, J.A., Benito, M.I., Díaz-Molina, M., Arenillas, I., 2014. Tidal influence in redbeds: a palaeoenvironmental and biochronostratigraphic reconstruction of the Lower Tremp Formation (South-Central Pyrenees, Spain) around the Cretaceous/Paleogene boundary. Sedimentary Geology 312, 31–49.

Donato, S.V., Reinhardt, E.G., Boyce, J.I., Pilarczyk, J.E., Jupp, B.P., 2009. Particle-size distribution of inferred tsunami deposits in Sur Lagoon, Sultanate of Oman. Marine Geology 257, 54–64.

Droser, M.L., Bottjer, D.J., 1986. A semiquantitative field classification of ichnofabric. Journal of Sedimentary Research 56.

Ehrenberg, S.N., Nadeau, P.H., Steen, Ø., 2009. Petroleum reservoir porosity versus depth: Influence of geological age. AAPG bulletin 93, 1281–1296.

Fürsich, F.T., Wilmsen, M., Seyed-Emami, K., Schairer, G., Majidifard, M.R., 2003. Platform-basin transect of a Middle to Late Jurassic large-scale carbonate platform system (Shotori Mountains, Tabas area, east-central Iran). Facies 48, 171–198.

Gaaloul, N., Amrouni, O., Heggy, E., Douss, N., Hzami, A., Khélifi, N., Bejaoui, B., Sánchez, A., 2022. Impacts of water stress on lagoonal ecosystem degradation in semi-arid coastal areas. Marine Pollution Bulletin 179, 113445. https://doi.org/10.1016/j.marpolbul.2022.113445

Ghinassi, M., Oms, O., Cosma, M., Finotello, A., Munari, G., 2021. Reading tidal processes where their signature is cryptic: The Maastrichtian meandering channel deposits of the Tremp Formation (Southern Pyrenees, Spain). Sedimentology 68, 2009–2042.

Hickson, T.A., Lamb, M., 2012. Microbial-Dominated Carbonate Sedimentation in Oligo-Miocene Transtensional Basins of the Lake Mead (Nevada) Region. AAPG Annual Convention and Exhibition, Long Beach, California, April 22-25, 2012.

Jahnert, R.J., Collins, L.B., 2013. Controls on microbial activity and tidal flat evolution in Shark Bay, Western Australia. Sedimentology 60, 1071–1099. https://doi.org/10.1111/sed.12023

Kendall, A.C., 1978. Facies models 11. Continental and supratidal (sabkha) evaporites. Geoscience Canada.

Krajewski, K.P., \Lącka, B., Kuźniarski, M., Or\lowski, R., Prejbisz, A., 2001. Diagenetic origin of carbonate in the Marhøgda Bed (Jurassic) in Spitsbergen, Svalbard. Polish Polar Research 22.

Macquaker, J.H., Curtis, C.D., Coleman, M.L., 1997. The role of iron in mudstone diagenesis; comparison of Kimmeridge Clay Formation mudstones from onshore and offshore (UKCS) localities. Journal of Sedimentary Research 67, 871–878.

Madany, I.M., Akhter, M.S., 1990. Assessment of the chemical and physical properties of adari spring in Bahrain. Environment International 16, 297–300. https://doi.org/10.1016/0160-4120(90)90124-O

McLennan, S.M., Hemming, S., McDaniel, D.K., Hanson, G.N., 1993. Geochemical approaches to sedimentation, provenance, and tectonics. Special Papers-Geological Society of America 21–21.
Mullins, H.T., Neumann, A.C., 1979. Deep carbonate bank margin structure and sedimentation in the northern Bahamas.
Nasiri, Y., Moussavi-Harami, R., Mahboubi, A., Mosaddegh, H., 2019. Sequence stratigraphic significance of shell concentrations in the Mobarak Formation (Mississippian), Alborz Zone, Northern Iran. N Jb Geol Palaont Abh 2, 171–195.
Palermo, D., Aigner, T., Nardon, S., Blendinger, W., 2010. Three-dimensional facies modeling of carbonate sand bodies: Outcrop analog study in an epicontinental basin (Triassic, southwest Germany). AAPG bulletin 94, 475–512.
Palit, K., Rath, S., Chatterjee, S., Das, S., 2022. Microbial diversity and ecological interactions of microorganisms in the mangrove ecosystem: Threats, vulnerability, and adaptations. Environmental Science and Pollution Research 29, 32467–32512.
Pearson, D., Weindorf, D.C., Chakraborty, S., Li, B., Koch, J., Van Deventer, P., de Wet, J., Kusi, N.Y., 2018. Analysis of metal-laden water via portable X-ray fluorescence spectrometry. Journal of Hydrology 561, 267–276. https://doi.org/10.1016/j.jhydrol.2018.04.014
Pierce, W.H., 1993. Southern Arabian Basin oil habitat: Seals and gathering areas, in: Middle East Oil Show. OnePetro.
Postel, J.-J., Mukhtar, A.N., Feugère, P., 2002. A successful 3-D seismic survey over Bahrain Island. GeoArabia 7, 657–672.
Powers, R.W., Ramirez, L.F., Redmond, C.D., Elberg, E.L., 1966. Geology of the Arabian peninsula. Geological survey professional paper 560, 1–147.
Qingyu, G., Baotian, P., Na, L., Qiong, L., Zhenbo, H., Hongshan, G., Shujian, X., Yong, W., 2010. An indicator of sand storms in the south of the Tengger Desert. Theor Appl Climatol 102, 197–203. https://doi.org/10.1007/s00704-010-0252-4
Quick, J.E., Bosch, P.S., 1990. Tectonic History of the Northern Nabitah Fault Zone, Arabian Shield, Kingdom of Saudi Arabia.
Reid, R.P., Andres, M.S., Bowlin, E.M., Jackson, K.L., Parke, E.C., 2012. Lessons Learned from Modern Marine Stromatolites, Bahamas. AAPG Hedberg Conference Microbial Carbonate Reservoir Characterization, Houston, Texas, 3-8 June 2012.
Reid, R.P., Gaspar, A.P.L., Bowlin, E.M., Custals, L., Andres, M.S., 2011. Microbialites and Sediments: A 2-Year Record of Burial and Exposure of Stromatolites and Thrombolites at Highborne Cay Bahamas. STROMATOLITES: Interaction of Microbes with Sediments 407–425. https://doi.org/10.1007/978-94-007-0397-1_18
Reinson, G.E., 1984. Barrier-island and associated strand-plain systems. Facies Models 119–140.
Rodriguez, A.B., Yu, W., Theuerkauf, E.J., 2018. Abrupt increase in washover deposition along a transgressive barrier island during the late nineteenth century acceleration in sea-level rise, in: Barrier Dynamics and Response to Changing Climate. Springer, pp. 121–145.
Ryer, T.A., Anderson, P.B., 2004. AAPG Studies in Geology No. 50,(Section Title: The Ferron Sandstone–Overview and Reservoir Analog) Chapter 3: Facies of the Ferron Sandstone, East-Central Utah.
Sabri, M.M., 2020. Chemical and Structural Analysis of Rocks Using X-ray Fluorescence and X-ray Diffraction Techniques. ARO 8, 79–87. https://doi.org/10.14500/aro.10643
Sarkar, U., Das, R.K., 2022. Contribution to the study of the paleoenvironmental evolution (Eocene) of the eastern part of Tethys: a comprehensive study from Prang Limestone, Meghalaya, India. J. Sediment. Environ. 7, 651–670. https://doi.org/10.1007/s43217-022-00114-6
Shaltami, O.R., Fares, F.F., Errishi, H., Oshebi, F.M.E., 2020. Isotope Geochronology of the Exposed Rocks in the Cyrenaica Basin, NE Libya. Springer Nature.

Sharland, P.R., Archer, R., Casey, D.M., Davies, R.B., Hall, S.H., Heward, A.P., Horbury, A.D., Simmons, M.D., 2001. Arabian Plate Sequence Stratigraphy. GeoArabia, Spec Publ 2, Gulf PetroLink. Oriental Press, Manama, Bahrain, 371p.
Shinn, E.A., 1983. Tidal flat environment. Carbonate depositional environments: AAPG Memoir 33, 172–210.
Thralls, W.H., Hasson, R.C., 1956. Geology and oil Resources of Eastern Saudi Arabia: 20 Congrso Geologico International, 2. Asia & Oceania.
Tucker, M.E., 1985. Shallow-marine carbonate facies and facies models. Geological Society, London, Special Publications 18, 147–169.
Tucker, M.E., Jones, S.J., 2023. Sedimentary petrology. John Wiley & Sons.
Walker, R.G., 2006. Facies Models Revisited, in: Posamentier, H.W., Walker, R.G. (Eds.), Facies Models Revisited. SEPM Society for Sedimentary Geology, p. 0. https://doi.org/10.2110/pec.06.84.0001
Weijermars, R., 1999. Surface geology, lithostratigraphy and Tertiary growth of the Dammam Dome, Saudi Arabia: a new field guide. GeoArabia 4, 199–226.
Weimer, R.J., Howard, J.D., Lindsay, D.R., 1982. Tidal Flats and Associated Tidal Channels: PART 1.
Wignall, P.B., Newton, R., Brookfield, M.E., 2005. Pyrite framboid evidence for oxygen-poor deposition during the Permian–Triassic crisis in Kashmir. Palaeogeography, Palaeoclimatology, Palaeoecology 216, 183–188.
Willis, R.P., 1967. Geology of the Arabian Peninsula-Bahrain (No. No. 560-E). United States Department of the Interior, Geological Survey.
Zhang, Y., Xue, C., Xue, Y., Gao, R., Zhang, X., 2005. Determination of the degree of deacetylation of chitin and chitosan by X-ray powder diffraction. Carbohydrate research 340, 1914–7. https://doi.org/10.1016/j.carres.2005.05.005
Zubari, W.K., 1999. The Dammam aquifer in Bahrain–Hydrochemical characterization and alternatives for management of groundwater quality. Hydrogeology Journal 7, 197–208.
Zubari, W.K., Khater, A.R., 1995. Brackish groundwater resources in Bahrain: Current exploitation, numerical evaluation and prospect for utilization. Water resources management 9, 277–297.

Figures captions

Figure 1. Location map of the study area: a) Bahrain island location with geological formation ages of the Arabian Peninsula (after Brown et al., 1989) ; b) Bahrain island map showing the location of the study area, geological exposed formations, and a simplified stratigraphic section of Bahrain's rock exposures adopted (after Postel et al., 2002; Willis, 1967); c) Study area geological map indicating the studied outcrop exposures.

Figure 2. Outcrop panoramic view of the Horse Racing Club (HRC) showing the Rus Formation exposure: a) the southern region of the study area withview towards N, width of view 180 m; b) the norther region of the study area with view towards the S, width of view 400 m.

Figure 3. Schematic cross-section showing the regional structural dip, the Awali Field area in relation to the study area. For the location of the cross-section, see Fig. 1-b.

Figure 4. A measured stratigraphic section of the exposed Rus Formation over the restricted Awali Field area represented by the Jabal Al Dukhan location and the HRC study area. See Fig. 3 for details of the HRC outcrop. The Shark Tooth Member was adopted after Abahussain (2015).

Figure 5. Detailed stratigraphic section representing the upper Rus Formation of the studied HRC outcrop area in Bahrain.

Figure 6. Thin section images in PPL (plane polarized light) of representative samples for F1–F4 facies: a) F1 facies, mudstone to wackestone, clotted micrite (CM), faint laminae (FL), associated peloidal fabric (P), hematite spots (H), and interparticle porosity (Po); b) F2 facies, mudstone to skeletal floatstone, angular micrite rip-ups (MR), hematite spots (H), secondary moldic porosity (MD), and angular lithoclasts embedded in micritic sediment (LC); c) F3 peloidal dolostone facies, packstone fabric, faint laminae (FL), foraminifera are absent, clotted micrites (CM), and common peloidal fabric (P); d–f) F4 foraminiferal dolostone facies, mudstone to floatstone texture with common large foraminifera, e.g., *Alveolina* (e) and *Nummulites* associated with pyrite (f).

Figure 7. Outcrop appearance of the F1–F4 facies: a) Exposure of the F1, F2, and F3 facies. View towards NE. Note the thin thickness of the F2 facies; b) Top view of an exposed bed of the F2 facies with angular lithoclasts, c) an *in situ* bivalve mold (F4), d) *Alveolina* floatstone (F4), e) two adjacent calcite geodes (F4), and f) dark chert nodules of F4.

Figure 8. Syndepositional faulting over the lower section of the exposed stratigraphy, reflecting normal and reverse displacement. a) Outcrop photo and b) schematic interpretation. View towards NW, width of view 7 m.

Figure 9. Thin section images in PPL of representative samples for the F4–F8 facies: a) F4 facies pyrite framboids concentrated inside *Alveolina* shells partially replacing and rimming the interior; b) Thin section through a fossilized mangrove branch, showing the internal structure of the mangrove plant at the lower right of the thin section and external sediments to the upper left with abundant foraminifera, and dolomite rhombohedrals of the F4 facies; c) Quartz pseudomorphs, showing the original needle-shaped aggregates after gypsum (F6 facies); d) Packstone F7 facies, characterized by leached foraminifera (FO), subangular lithoclasts (LC), and clotted micrite fabric (CM); e) The mudstone F8 facies with a mangrove rootlet (rhizolith). The rhizolith interpretation is supported by the angular internal structure of the elongated object and the compacted sediments near the object's external wall; f) Clay material of the F8 facies being injected between dolomite grains and rhombohedrals.

Figure 10. Outcrop exposure photo panel of the F4 facies: a) An *in situ* fossilized mangrove bifurcating trunk. View towards W, field of view 2 m; b-c) Well-preserved fossilized mangrove forest associated with *rhizoliths*; d) Deformed beds reflecting a water escape structure. View towards W, field of view 5 m.

Figure 11. Outcrop exposure photo panel: a) Injectites across claystone facies. View towards NE (F5); b) Quartz pseudomorphs after gypsum; c) Halite layer embedded within the F5 facies; d) 0.5-m-thick evaporitic deposits composed of quartz pseudomorphs after gypsum (57% quartz and 43% dolomite). View towards SE; e) Evaporitic limited lateral extent capping the small hill. View towards SE, width of view 40 m; f) The argillaceous dolostone facies (F7) and zoom in to (g), showing *Ophiomorpha* burrows filled with clay material. View towards SE.

Figure 12. Outcrop exposure photo panel: a) The marl facies (F8) with a display of lateral accretion surfaces marked by oxidized laminae. View towards SE, width of view 5 m; b) Fossil-rich beds of the F8 facies, with a zoom in showing a bivalve shell fragment in (c) and nummulites in (d); g) The bioturbated chalky dolostone facies (F9), showing the bottom view of a large burrow (black arrow) associated with a distinct *Thalassinoides* boxwork; e) The generalized F9 facies bed geometry, characterized by flat tops and an erosional base. View towards NE; f) A *Thalassinoides* burrow example in the F9 facies (black arrow); h) The cross-bedded dolostone facies (F10), dominated by *Ophiomorpha* burrows (black arrow); i) Lateral pinchout and discontinuity of the F10 facies (black arrow). View towards SW, width of view 5 m.

Figure 13. Thin section images in PPL of representative samples for the F9 and F10 facies: a) The peloidal wackestone to packstone facies (F9), common unidentified leached foraminifera shells (UN) expressing moldic porosity, and peloidal fabric (P); b) Grainstone texture of the F10 facies, moderately sorted grains that are composed of foraminifera, echinoderm spines, shell fragments, concentric ooids, fecal pellets, well-rounded to sub-angular quartz grains, and common intraparticle porosity (17%); c) F10 fecal pellets, detrital angular to subangular quartz, and concentric ooids; d) Concentric ooids and foraminifera; e) Zoom in on an echinoid spine; f) Extensively leached carbonate grains over the F10 facies.

Figure 14. Outcrop exposure photo panel: a) Grainstone lens of the F10 facies associated with faint trough cross-bedding that is visible towards the right. View towards W. Cross-bedding measurements indicate a western paleoflow direction. Back scale 13.5 cm in length; b) Trough cross-bedding of the F10 facies. Back triangle 13.5 cm in scale. Cross-bedding measurements indicate a SE paleoflow direction. View towards SW; c) Outcrop view of a continuous microbial bed of the F11 facies. View towards SE; d)

Stromatolitic wavy laminae that are associated with thrombolites towards the base (F11 facies); e) The bedded dolostone F12 facies, reflecting syndepositional microfaulting; f) A closeup view of the basal part of the F12 facies, showing fine to medium sub-rounded detrital grains, mostly represented by quartz, in a dolomitic white background.

Figure 15. Thin section images in PPL of representative samples for the F11–F13 facies: a) The microbial dolostone F11 facies, characterized by leaching enhancement (fenestral porosity), micritization, peloids, and faint micritic laminae; b) The laminated microbial dolostone F11 facies, characterized by repetitive alternation of micrite and peloidal micrite associated with fenestral porosity on the bottom right; c) The microbial wackestone texture of the F11 facies, thinly laminated (on average 0.25 mm) (L), fenestral porosity (F), peloidal fabric (P), foraminifera (MI), and a complete Ostracoda carapace shell and fragments (OR); d) The microbial floatstone F11 facies, clotted micritic fabric (MC) that exhibits fine to very fine rounded grains (GR), peloidal fabric (P), and a foraminifera fragment (Or); e) Microbial floatstone texture, clotted micritic fabric (MC) with subrounded grains (GR), dark brown to black hematite spots (H), and a microspheric foraminifera (*Alveolina*) fragment (Fr); f) The microbial wackestone F11 facies, brecciated peloidal grains, fenestral, and intergranular porosities; g) The wackestone to packstone F12 facies, common unidentified leached foraminifera shells (UN), rare dark hematite spots (H), and lithoclasts (LC); h) The mudstone to wackestone F13 facies, displaying a water escape structure (ES). The wackestone facies (WK) is associated with quartz silt size detrital grains that appear to be injected in the darker colored mudstone dominated facies (MS). White arrows indicate the flow direction.

Figure 16. Photo panel of the outcrop exposure: a) Syndepostional deformation associated with the contacts between the F5, F3, and F12 facies. View towards S; b) General view of the F12, F13, and F11 facies. View towards NW, width of view 14 m; c) Side view of inclined clinoformal beds; d) Top view of clinoformal beds, resembling beach ridges. View towards W.

Figure 17. Relationships between several major and trace elements, showing mostly positive relationships, except for Si/Ca, which displays a negative correlation.

Figure 18. Facies model for exposures of the Bahrain Rus Formation. For legend, see Fig. 5.

Figure 19. Paleogeographic reconstruction of the Early Eocene Rus Formation in the area covering Bahrain, the Eastern Province of Saudi Arabia, and Qatar.

Table caption

Table 1. Summary table of facies and facies associations, including mineral composition and porosity measurements for each facies.

Appendix A caption

Appendix A: Elemental analysis performed on 32 samples.

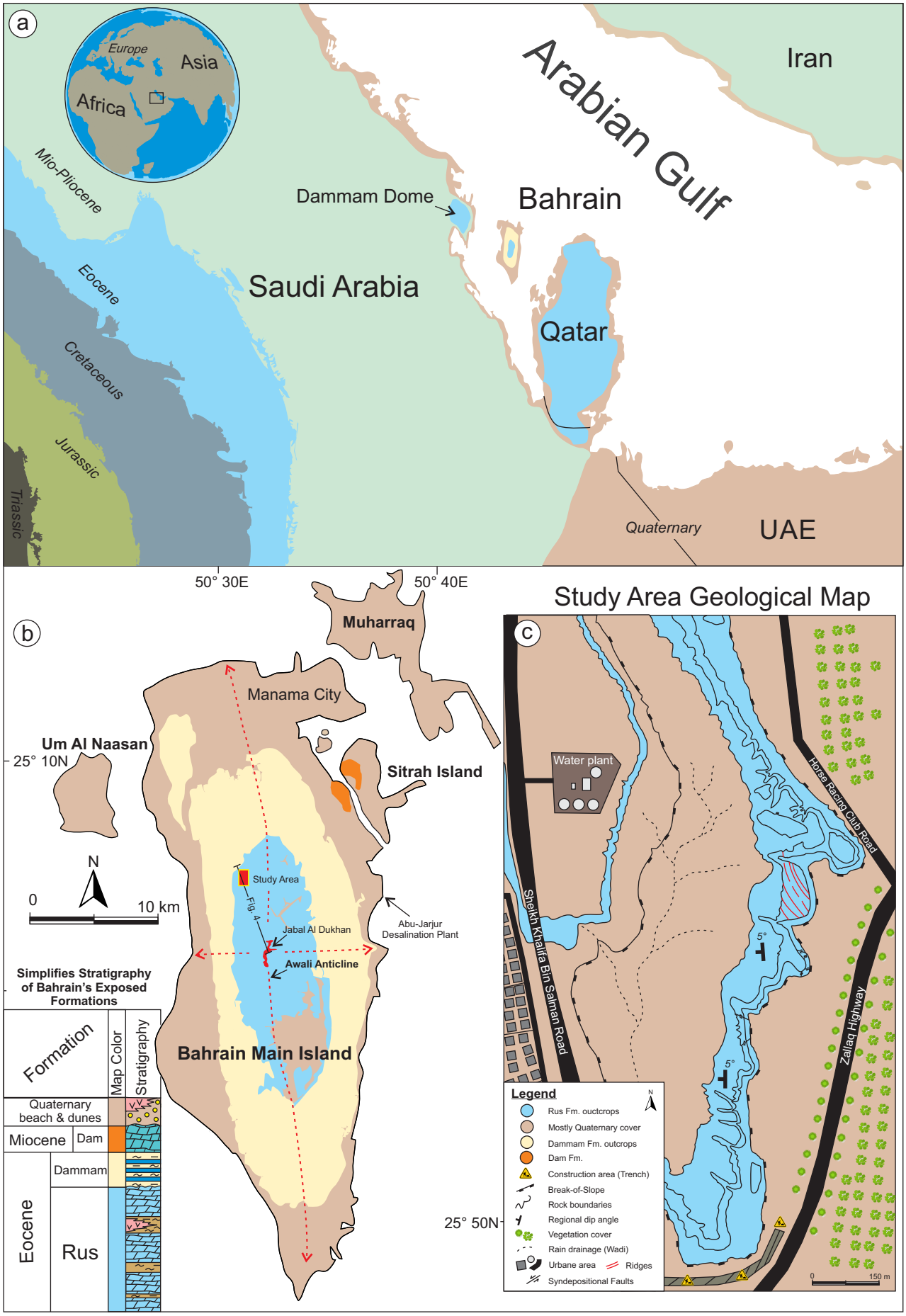
a
Europe
Asia
Africa
Iran
Arabian Gulf
Mio-Pliocene
Dammam Dome
Bahrain
Eocene
Saudi Arabia
Cretaceous
Qatar
Jurassic
Triassic
Quaternary
UAE
50° 30E
50° 40E
b
Muharraq
Manama City
Um Al Naasan
25° 10N
Sitrah Island
N
0
10 km
Study Area
Fig. 4
Jabal Al Dukhan
Abu-Jarjur
Desalination Plant
Awali Anticline
Bahrain Main Island
Simplifies Stratigraphy
of Bahrain's Exposed
Formations
Formation
Map Color
Stratigraphy
Quaternary
beach & dunes
Miocene
Dam
Eocene
Dammam
Rus
Study Area Geological Map
c
Water plant
Horse Racing Club Road
Sheikh Khalifa Bin Salman Road
Zallaq Highway
5°
25° 50N
Legend
Rus Fm. ouctcrops
Mostly Quaternary cover
Dammam Fm. outcrops
Dam Fm.
Construction area (Trench)
Break-of-Slope
Rock boundaries
Regional dip angle
Vegetation cover
Rain drainage (Wadi)
Urbane area
Ridges
Syndepositional Faults
0
150 m

FigurFe 1

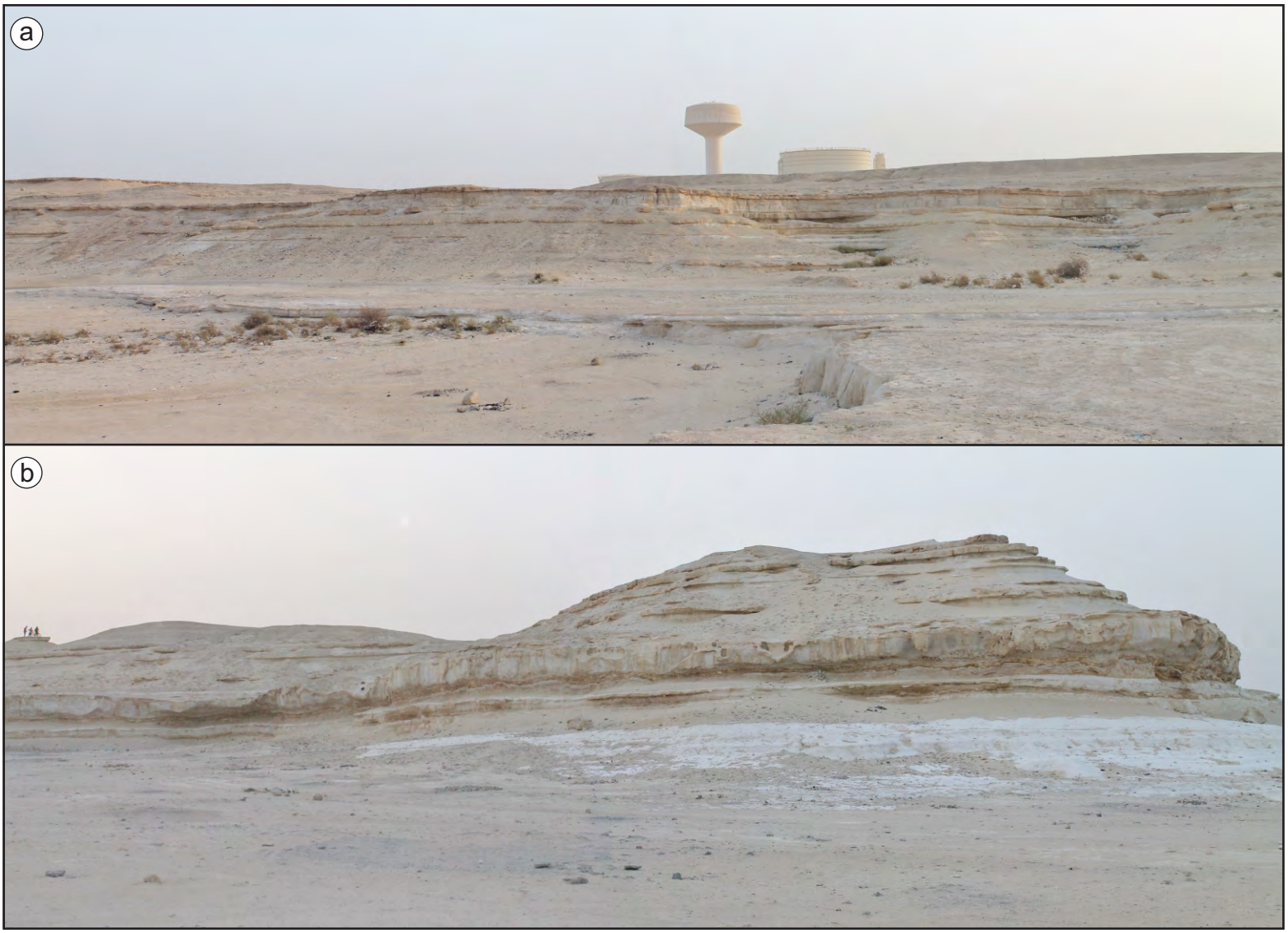

Figure 2

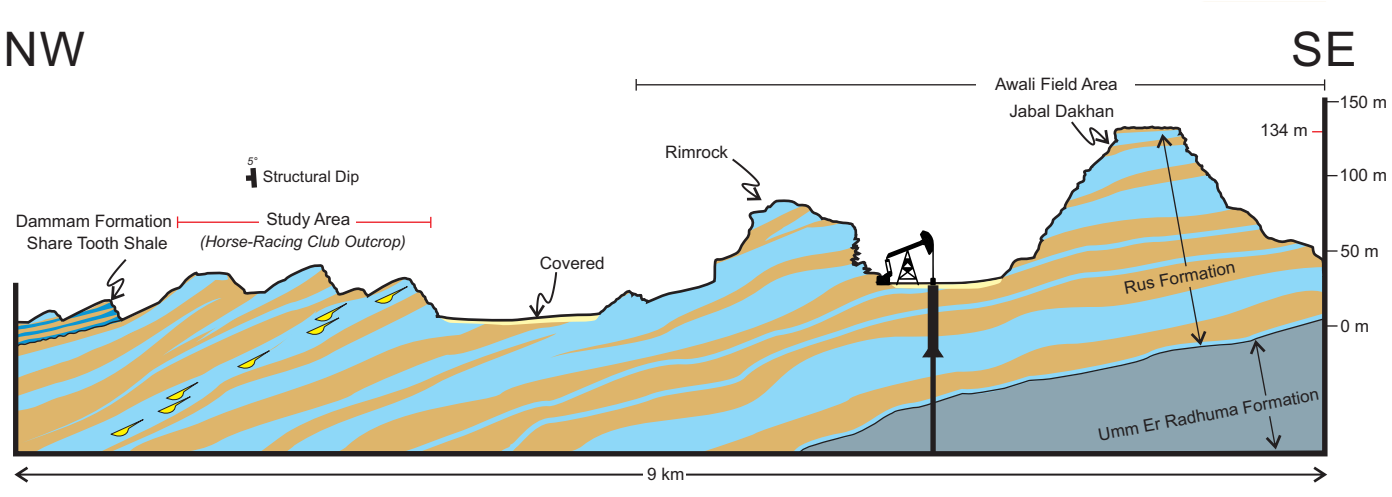
NW
SE
Awali Field Area
Jabal Dakhan
150 m
134 m
100 m
50 m
0 m
Rimrock
5°
Structural Dip
Dammam Formation
Share Tooth Shale
Study Area
(Horse-Racing Club Outcrop)
Covered
Rus Formation
Umm Er Radhuma Formation
9 km

Figure 3

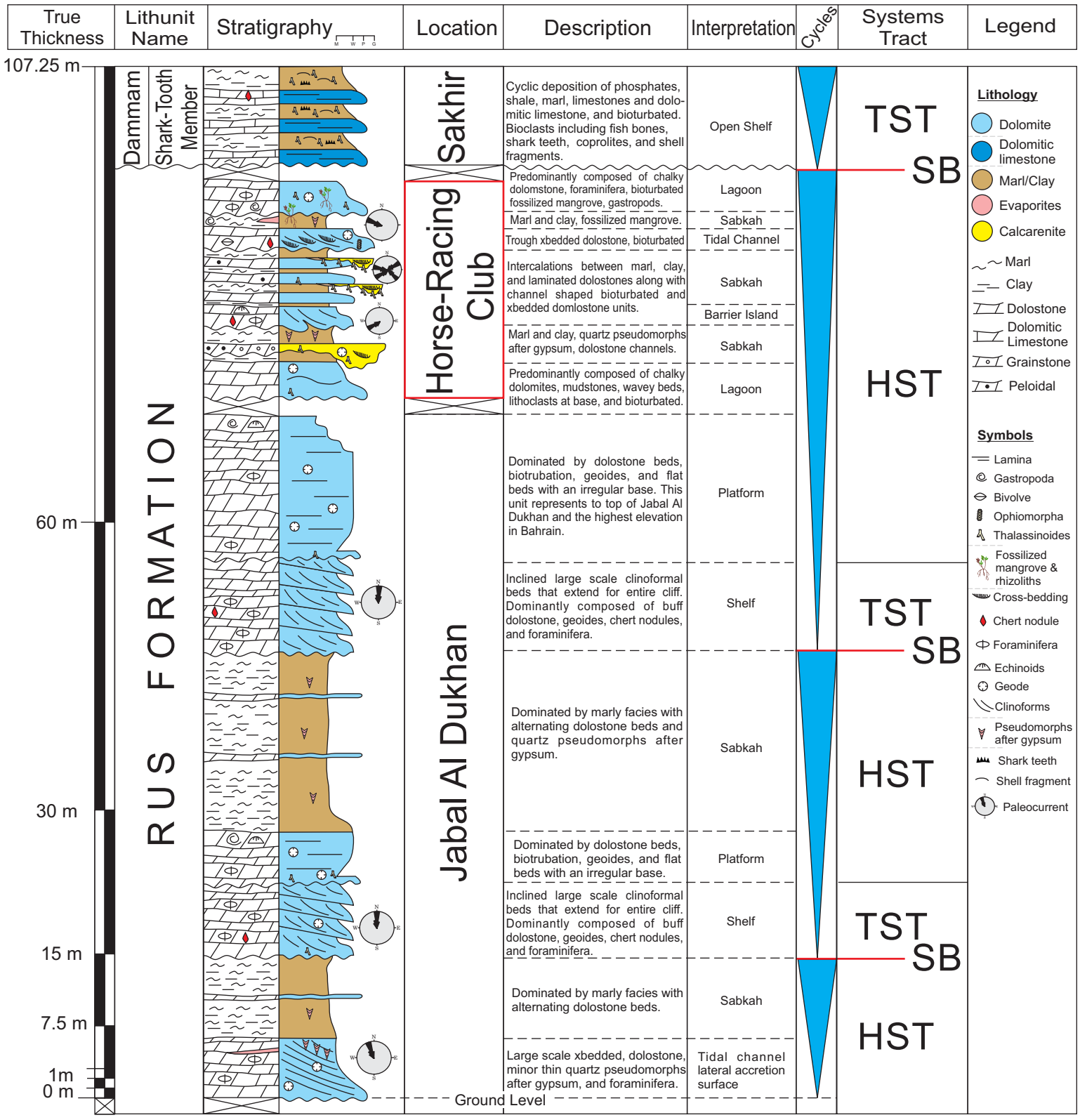
True Thickness
Lithunit Name
Stratigraphy
Location
Description
Interpretation
Cycles
Systems Tract
Legend
107.25 m
60 m
30 m
15 m
7.5 m
1m
0 m
Dammam
Shark-Tooth Member
RUS FORMATION
Sakhir
Horse-Racing Club
Jabal Al Dukhan
Cyclic deposition of phosphates, shale, marl, limestones and dolomitic limestone, and bioturbated. Bioclasts including fish bones, shark teeth, coprolites, and shell fragments.
Predominantly composed of chalky dolomstone, foraminifera, bioturbated fossilized mangrove, gastropods.
Marl and clay, fossilized mangrove.
Trough xbedded dolostone, bioturbated
Intercalations between marl, clay, and laminated dolostones along with channel shaped bioturbated and xbedded domlostone units.
Marl and clay, quartz pseudomorphs after gypsum, dolostone channels.
Predominantly composed of chalky dolomites, mudstones, wavey beds, lithoclasts at base, and bioturbated.
Dominated by dolostone beds, biotrubation, geoides, and flat beds with an irregular base. This unit represents to top of Jabal Al Dukhan and the highest elevation in Bahrain.
Inclined large scale clinoformal beds that extend for entire cliff. Dominantly composed of buff dolostone, geoides, chert nodules, and foraminifera.
Dominated by marly facies with alternating dolostone beds and quartz pseudomorphs after gypsum.
Dominated by dolostone beds, biotrubation, geoides, and flat beds with an irregular base.
Inclined large scale clinoformal beds that extend for entire cliff. Dominantly composed of buff dolostone, geoides, chert nodules, and foraminifera.
Dominated by marly facies with alternating dolostone beds.
Large scale xbedded, dolostone, minor thin quartz pseudomorphs after gypsum, and foraminifera.
Ground Level
Open Shelf
Lagoon
Sabkah
Tidal Channel
Sabkah
Barrier Island
Sabkah
Lagoon
Platform
Shelf
Sabkah
Platform
Shelf
Sabkah
Tidal channel lateral accretion surface
TST
SB
HST
TST
SB
HST
TST
SB
HST
Lithology
Dolomite
Dolomitic limestone
Marl/Clay
Evaporites
Calcarenite
Marl
Clay
Dolostone
Dolomitic Limestone
Grainstone
Peloidal
Symbols
Lamina
Gastropoda
Bivolve
Ophiomorpha
Thalassinoides
Fossilized mangrove & rhizoliths
Cross-bedding
Chert nodule
Foraminifera
Echinoids
Geode
Clinoforms
Pseudomorphs after gypsum
Shark teeth
Shell fragment
Paleocurrent

Figure 4

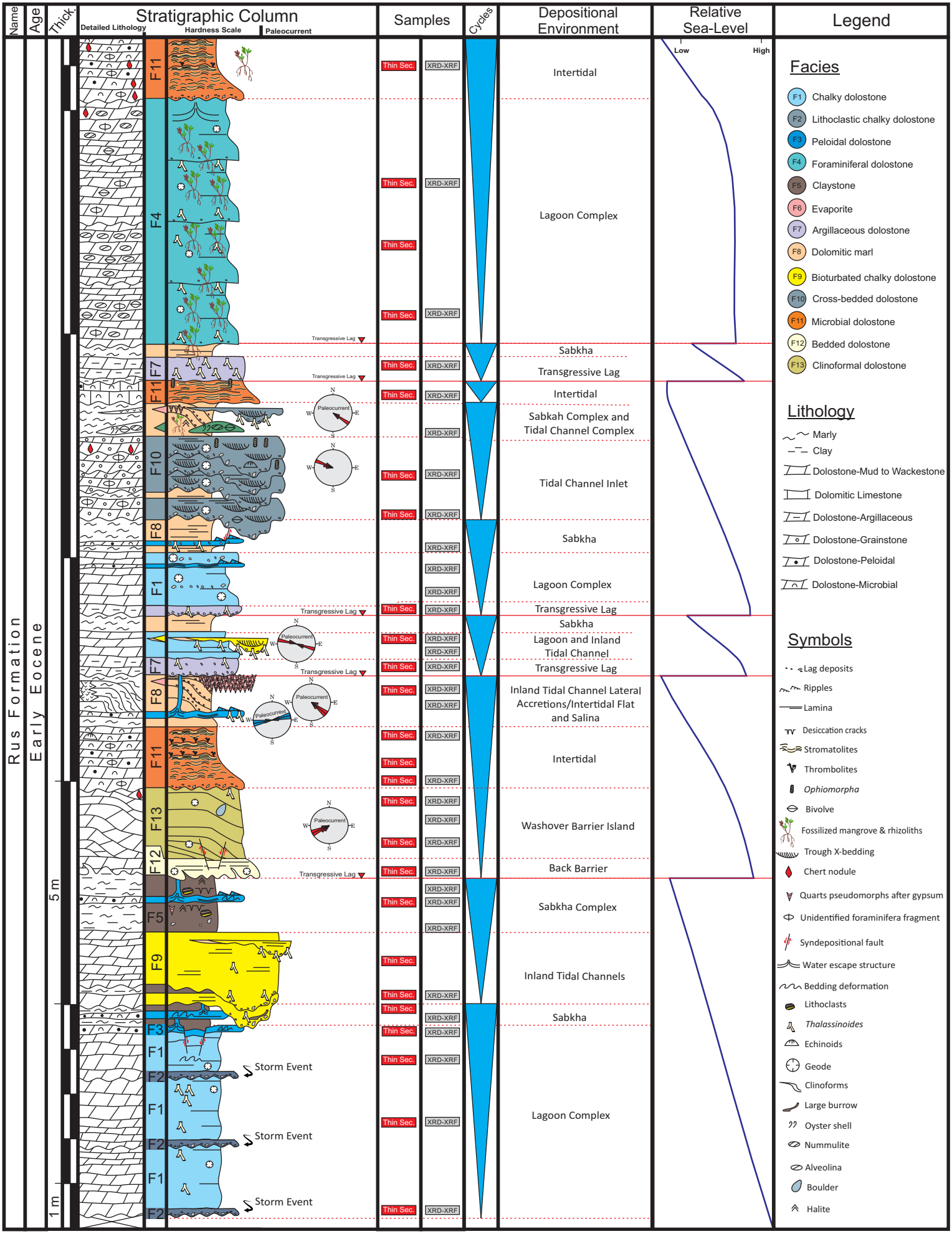
Name
Age
Thick.
Stratigraphic Column
Detailed Lithology
Hardness Scale
Paleocurrent
Samples
Cycles
Depositional Environment
Relative Sea-Level
Low
High
Legend
Rus Formation
Early Eocene
5 m
1 m
Thin Sec.
XRD-XRF
Transgressive Lag
Paleocurrent
Storm Event
Intertidal
Lagoon Complex
Sabkha
Transgressive Lag
Sabkah Complex and Tidal Channel Complex
Tidal Channel Inlet
Lagoon and Inland Tidal Channel
Inland Tidal Channel Lateral Accretions/Intertidal Flat and Salina
Washover Barrier Island
Back Barrier
Sabkha Complex
Inland Tidal Channels
Facies
F1 Chalky dolostone
F2 Lithoclastic chalky dolostone
F3 Peloidal dolostone
F4 Foraminiferal dolostone
F5 Claystone
F6 Evaporite
F7 Argillaceous dolostone
F8 Dolomitic marl
F9 Bioturbated chalky dolostone
F10 Cross-bedded dolostone
F11 Microbial dolostone
F12 Bedded dolostone
F13 Clinoformal dolostone
Lithology
Marly
Clay
Dolostone-Mud to Wackestone
Dolomitic Limestone
Dolostone-Argillaceous
Dolostone-Grainstone
Dolostone-Peloidal
Dolostone-Microbial
Symbols
Lag deposits
Ripples
Lamina
Desiccation cracks
Stromatolites
Thrombolites
Ophiomorpha
Bivolve
Fossilized mangrove & rhizoliths
Trough X-bedding
Chert nodule
Quarts pseudomorphs after gypsum
Unidentified foraminifera fragment
Syndepositional fault
Water escape structure
Bedding deformation
Lithoclasts
Thalassinoides
Echinoids
Geode
Clinoforms
Large burrow
Oyster shell
Nummulite
Alveolina
Boulder
Halite

Figure 5

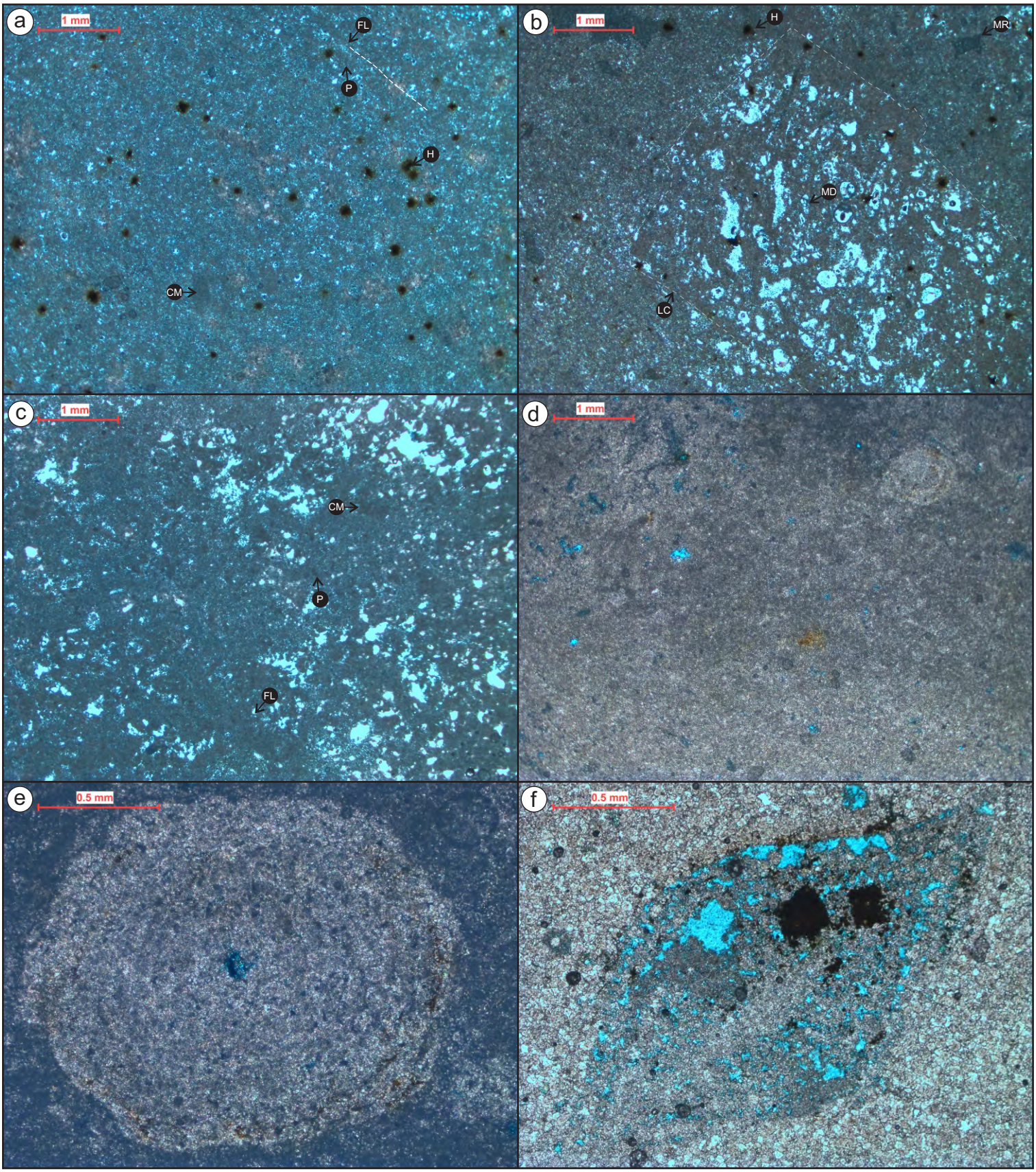

Figure 6

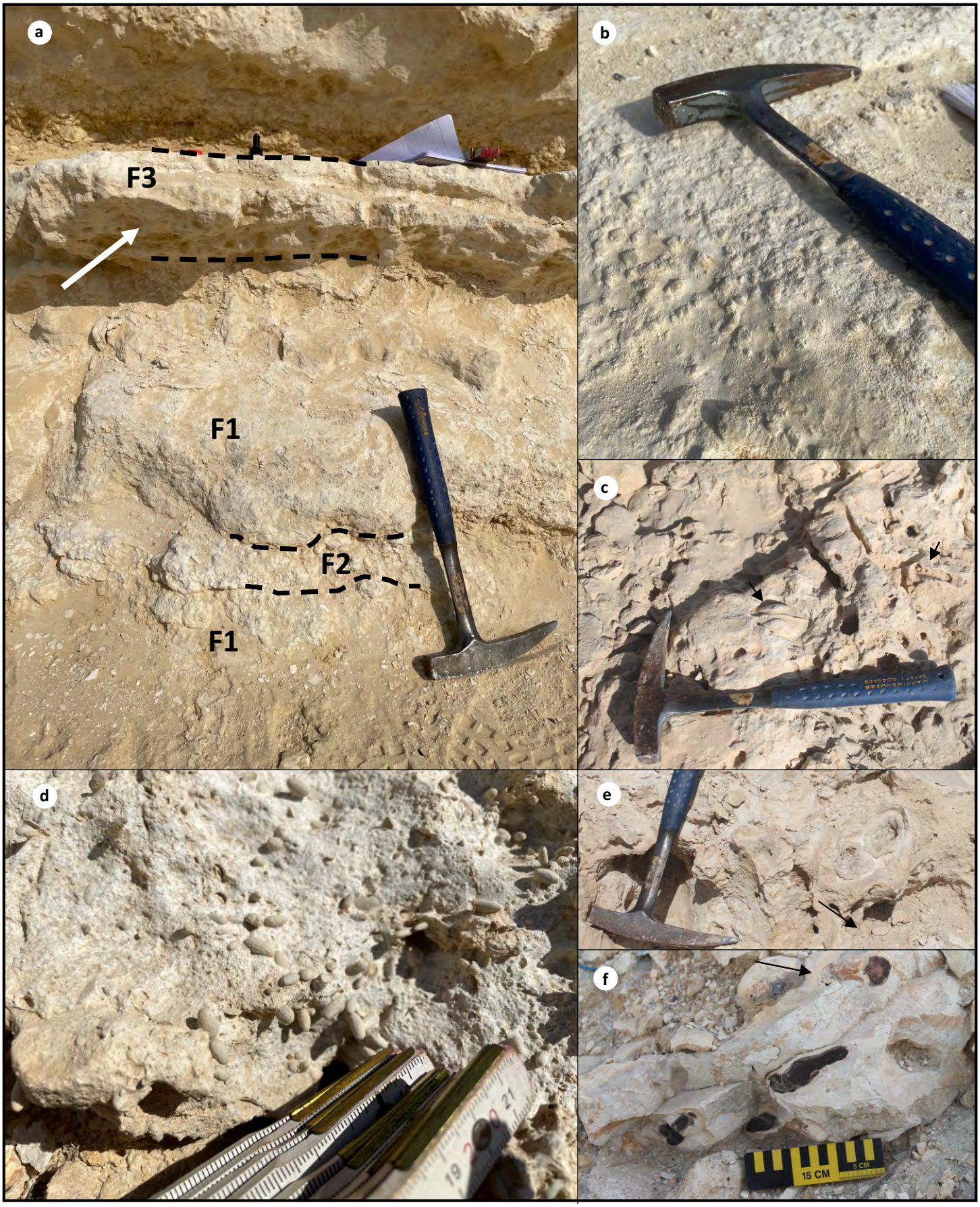

Figure 7

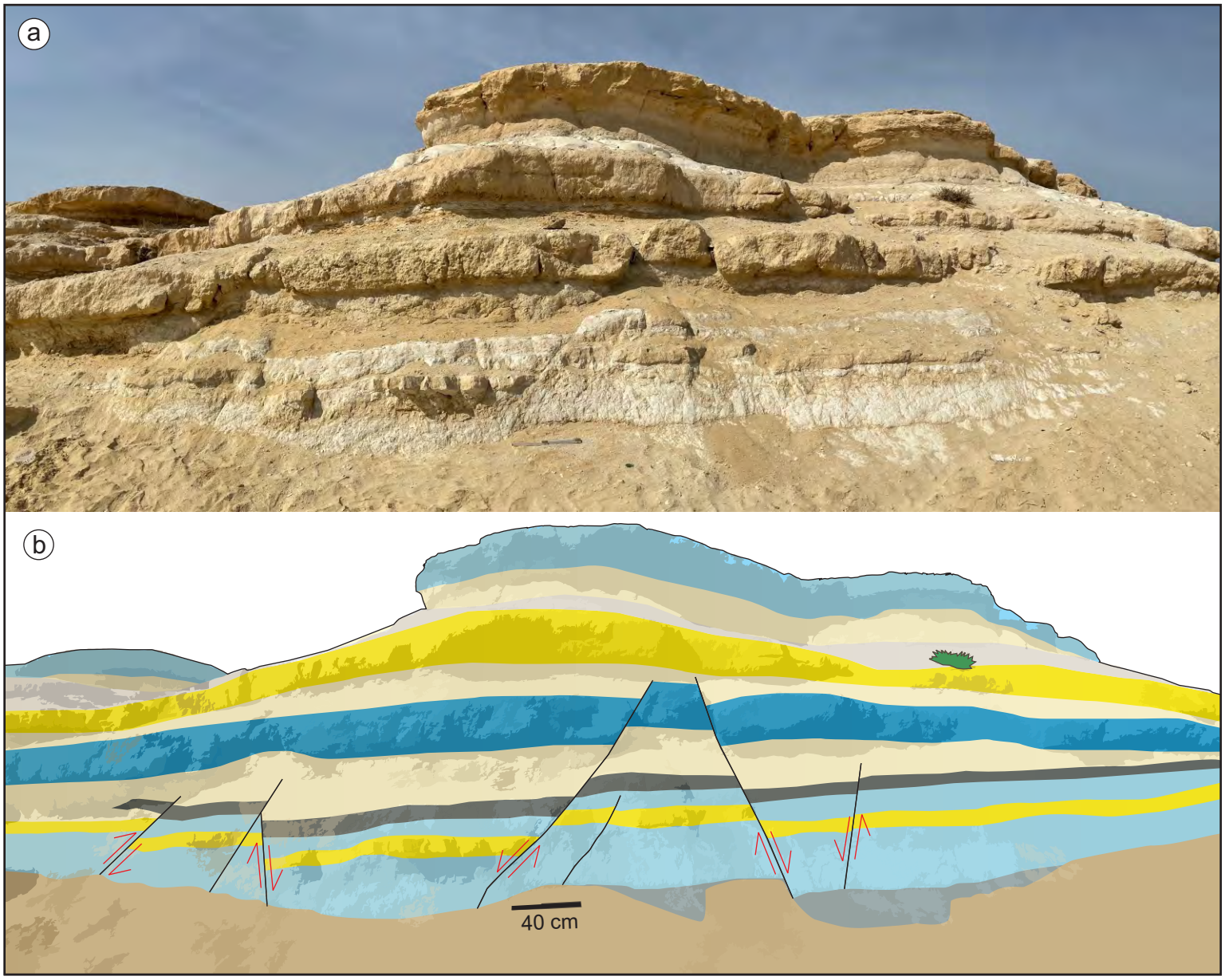

Figure 8

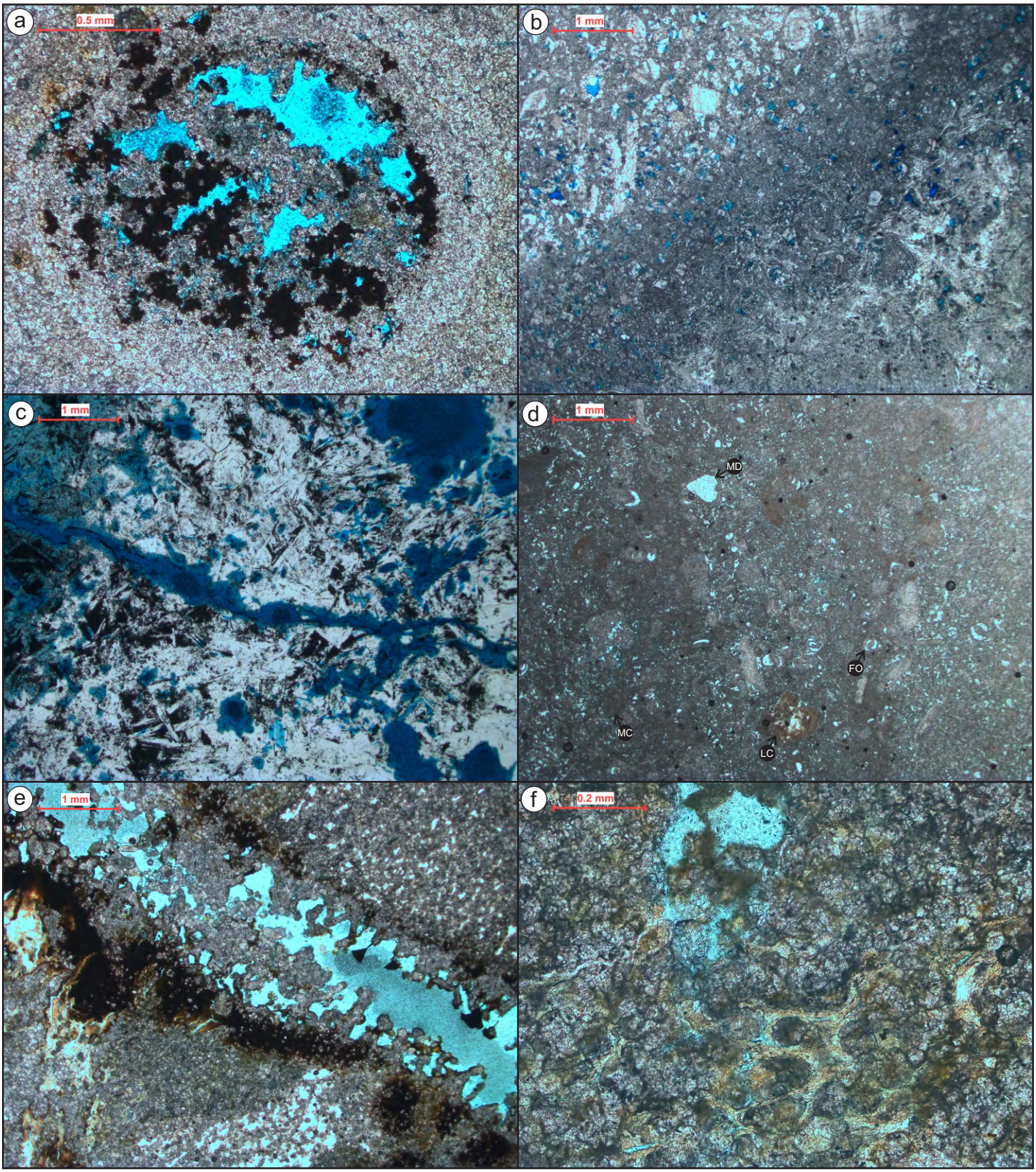

Figure 9

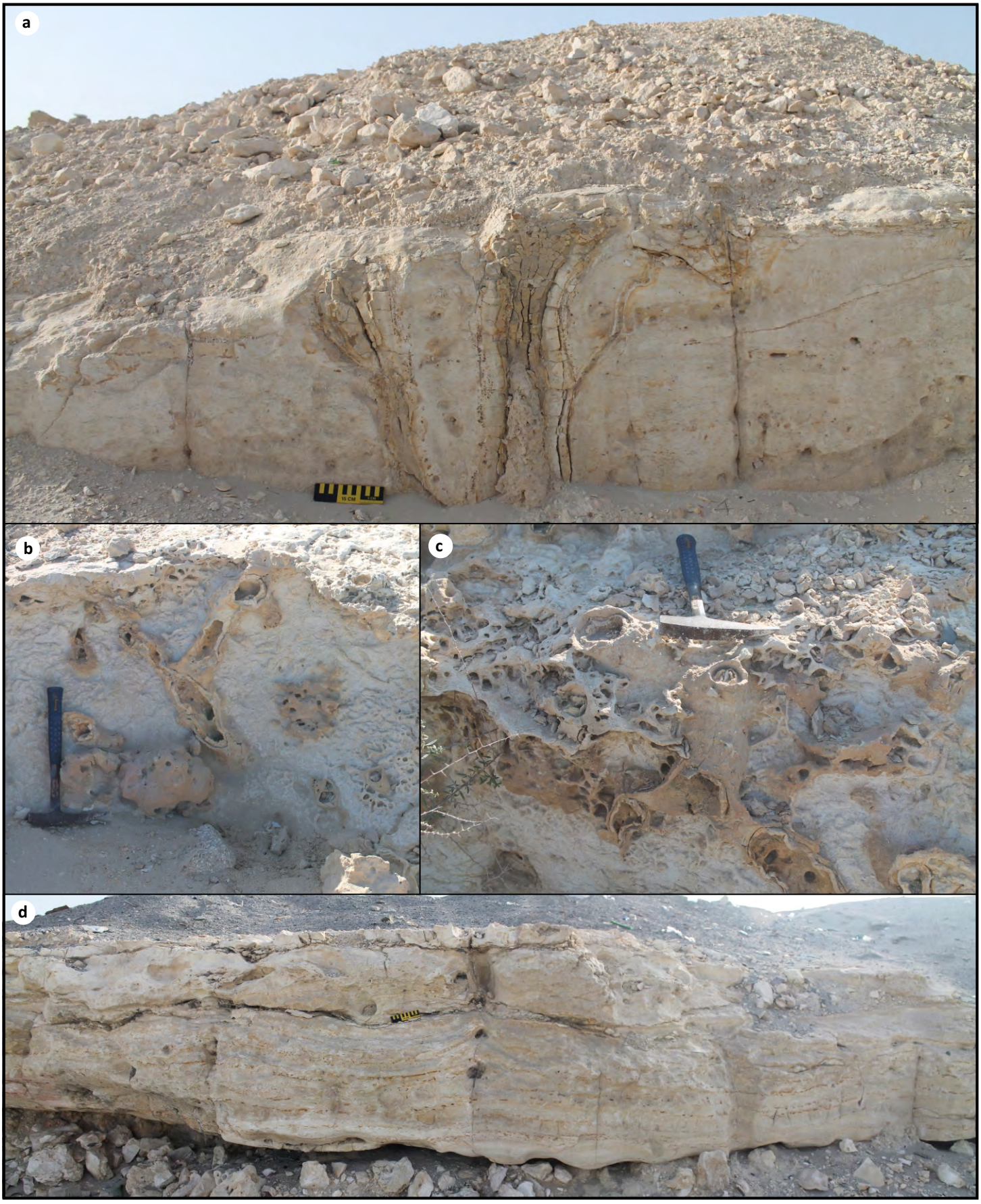

Figure 10

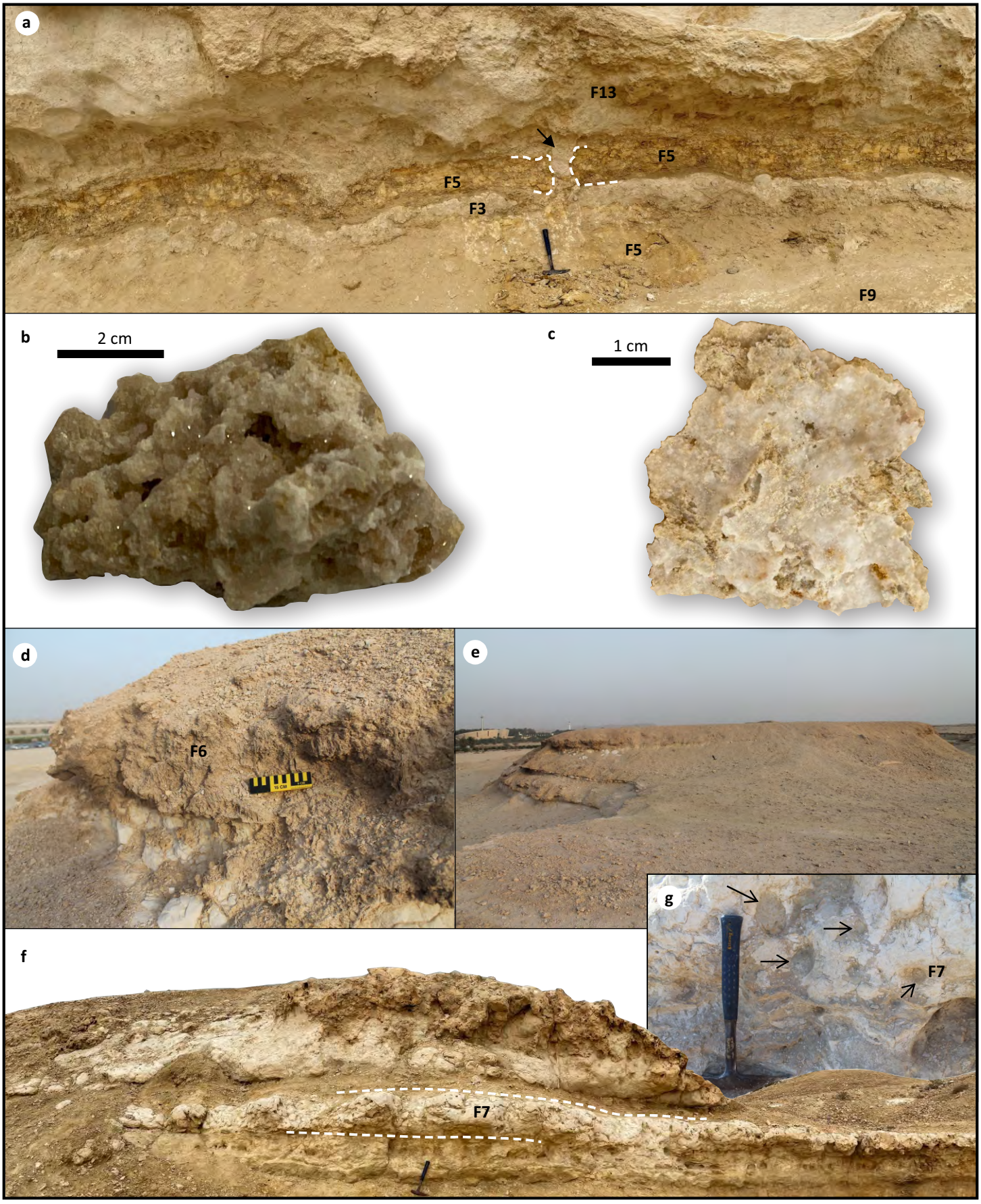

Figure 11

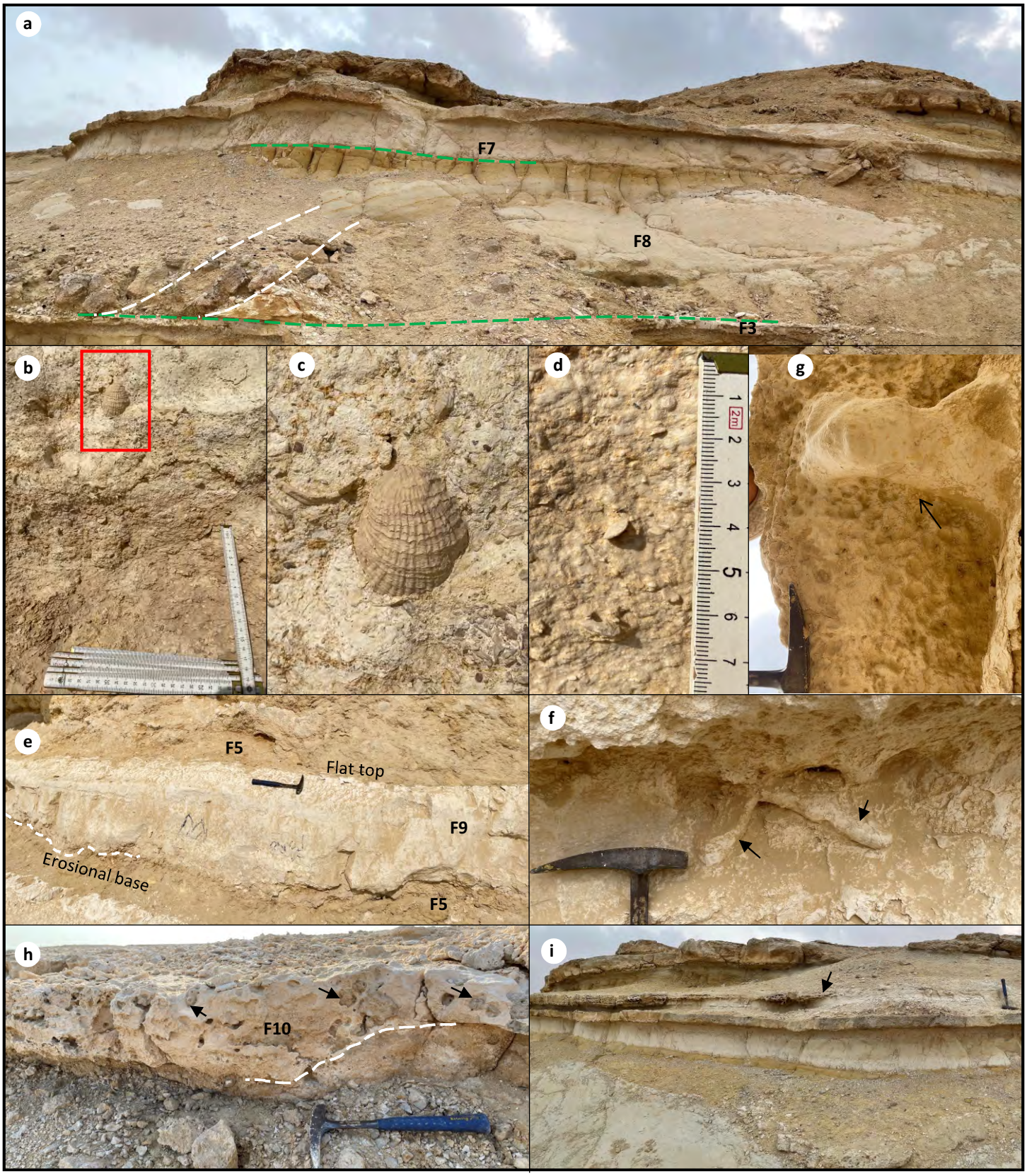

Figure 12

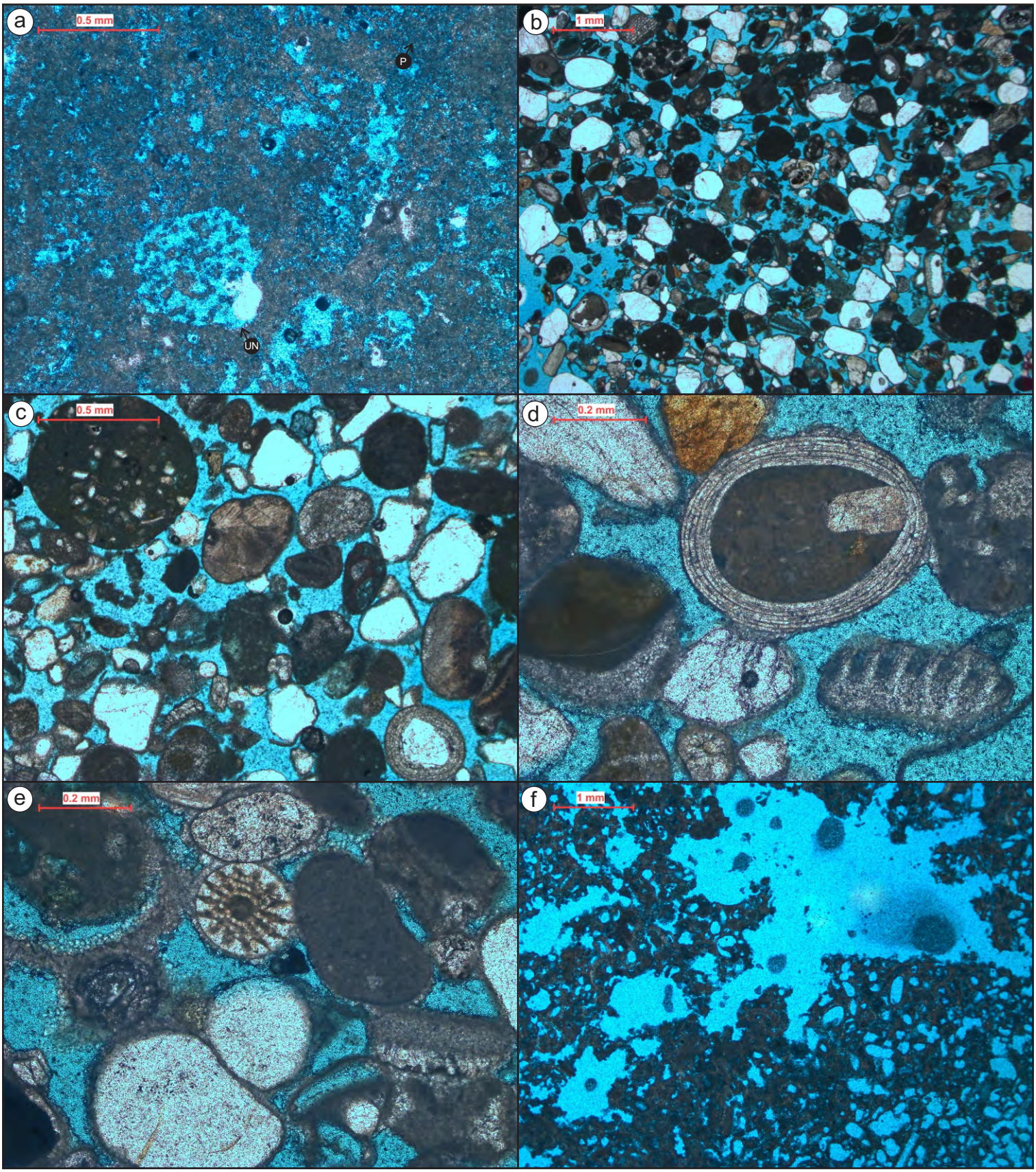

Figure 13

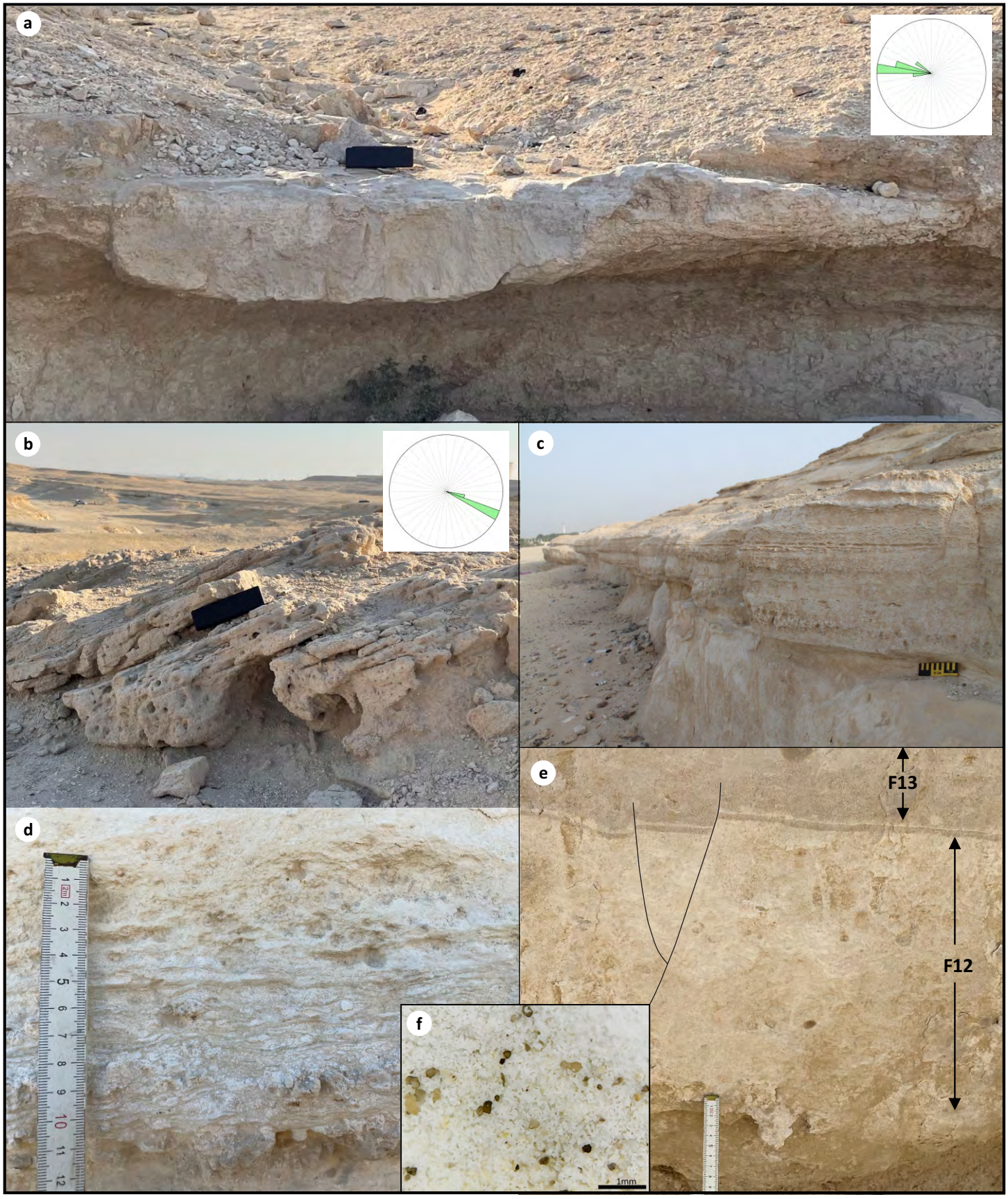

Figure 14

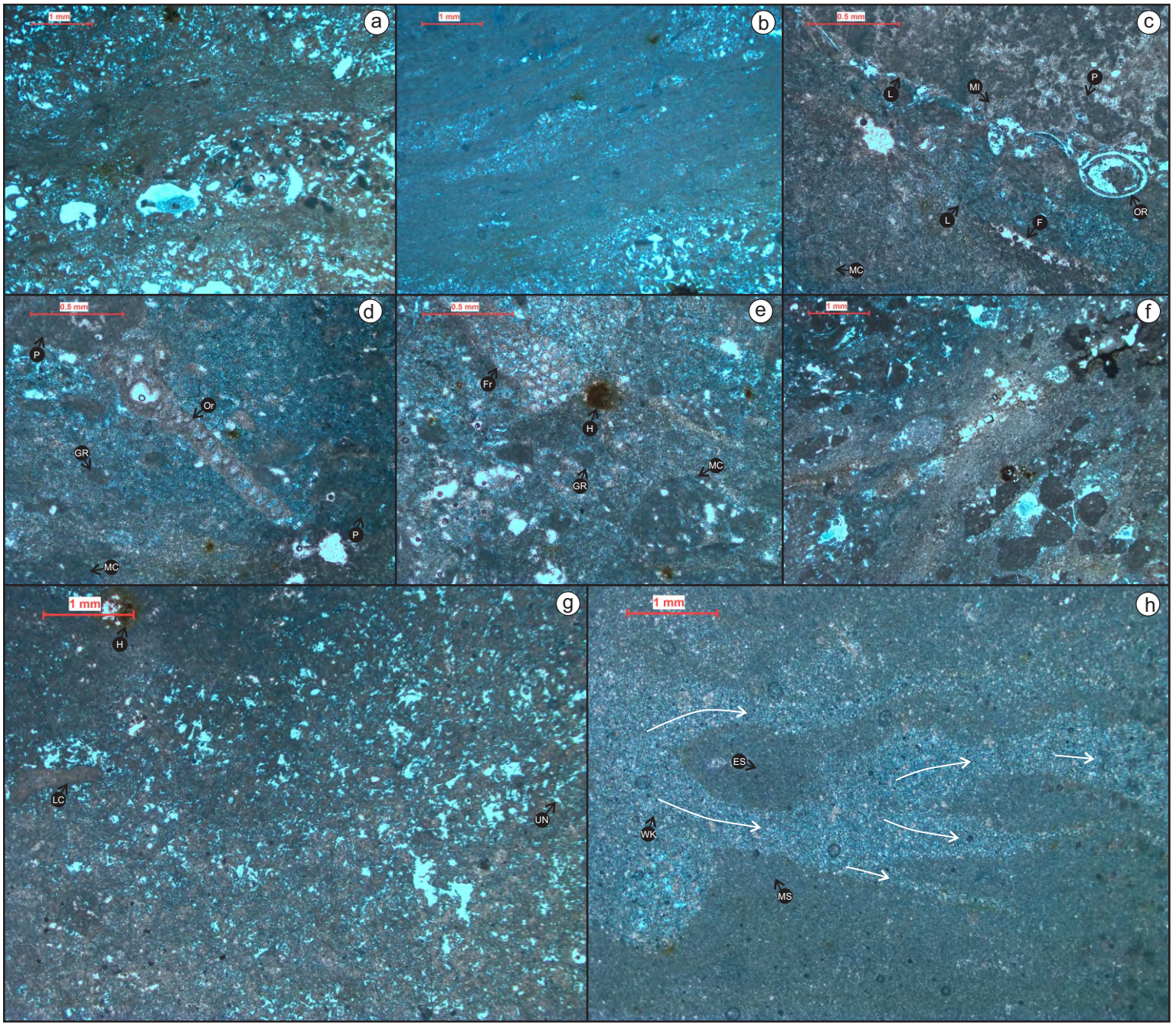
a
1 mm
b
1 mm
c
0.5 mm
L
MI
P
OR
L
F
MC
d
0.5 mm
P
Or
GR
P
MC
e
0.5 mm
Fr
H
GR
MC
f
1 mm
g
1 mm
H
LC
UN
h
1 mm
ES
WK
MS

Figure 15

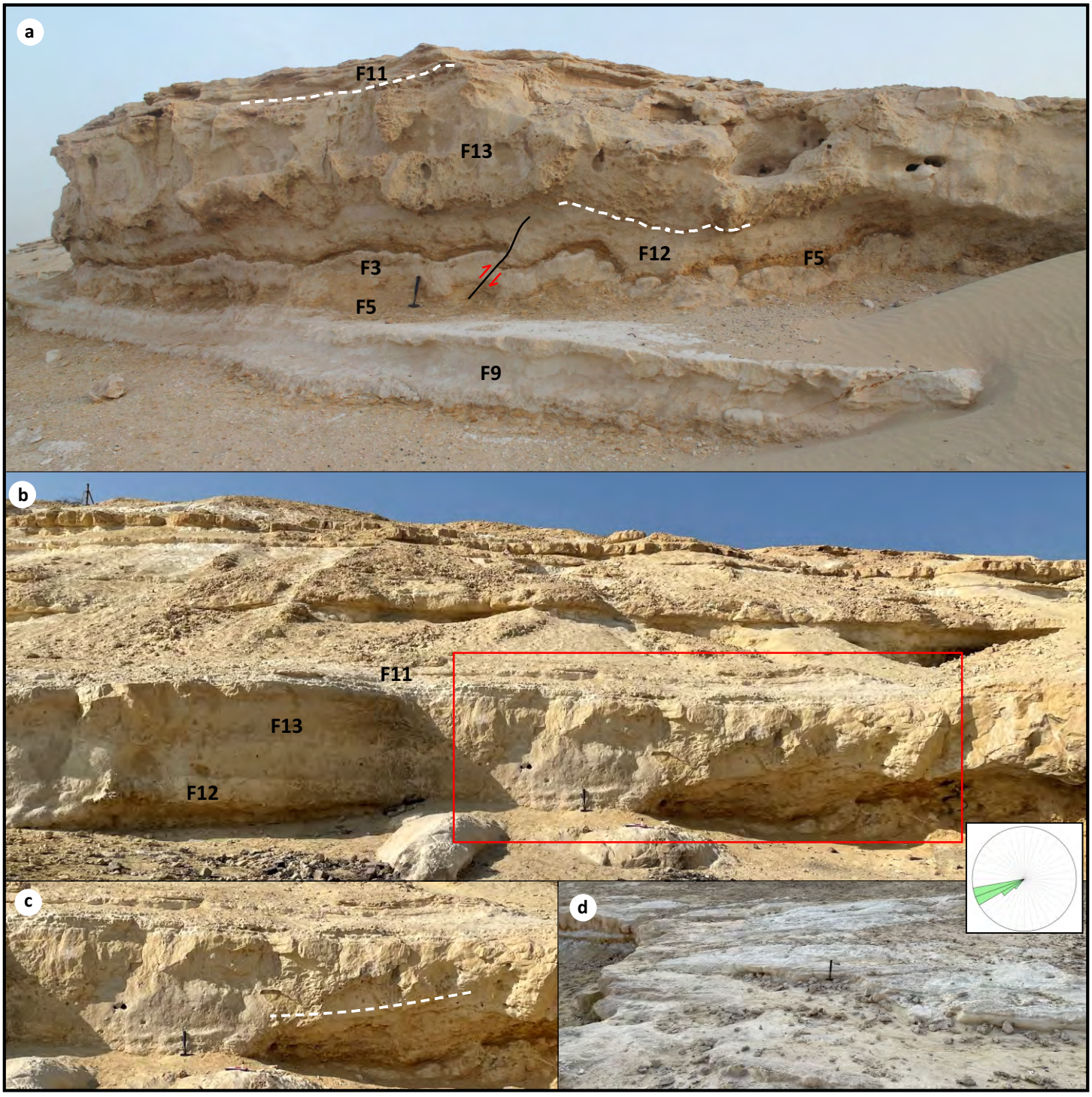

Figure 16

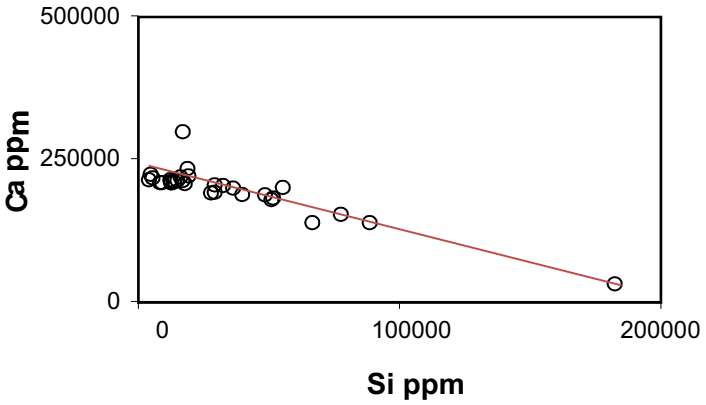
500000
250000
0
Ca ppm
0
100000
200000
Si ppm

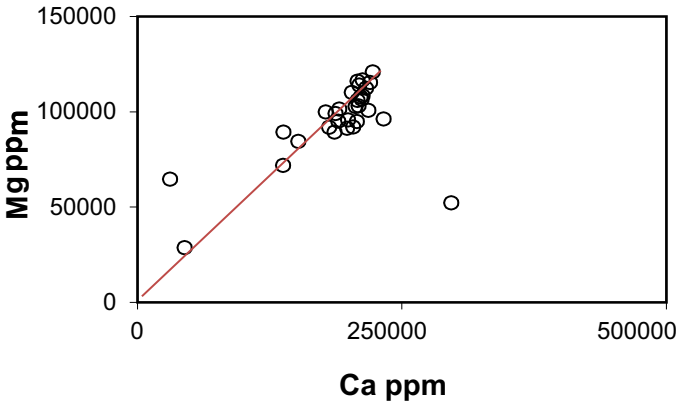
150000
100000
50000
0
Mg ppm
0
250000
500000
Ca ppm

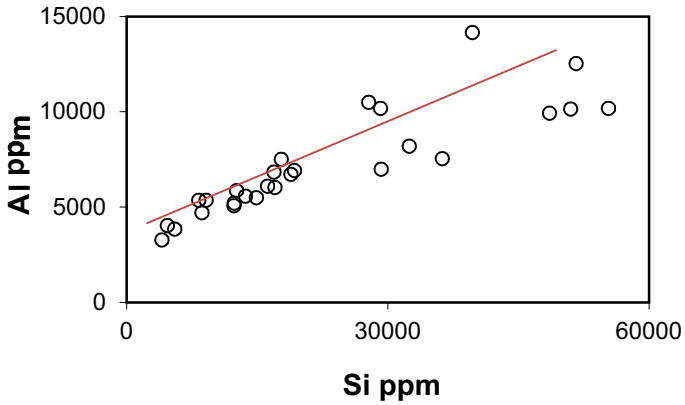
15000
10000
5000
0
Al ppm
0
30000
60000
Si ppm

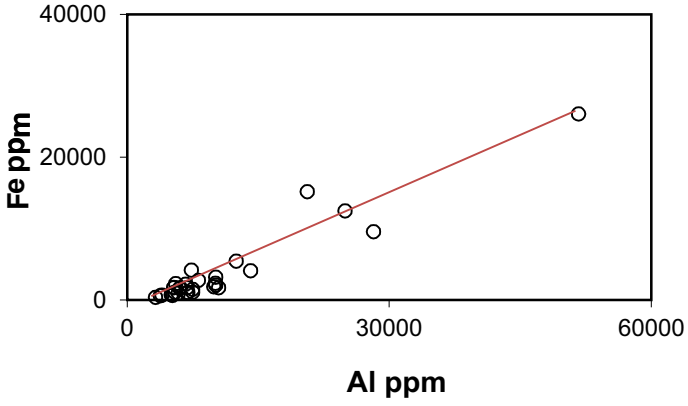
40000
20000
0
Fe ppm
0
30000
60000
Al ppm

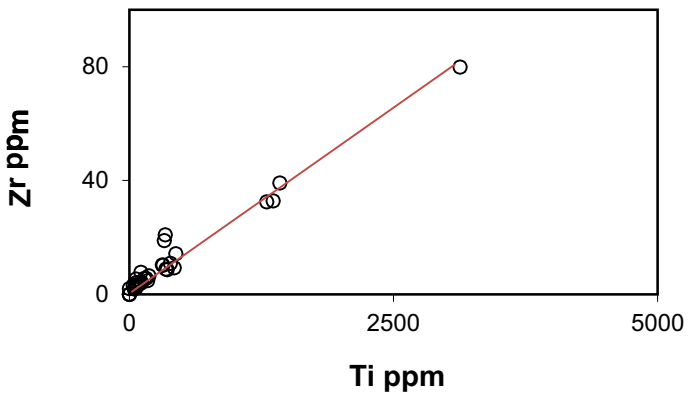
80
40
0
Zr ppm
0
2500
5000
Ti ppm

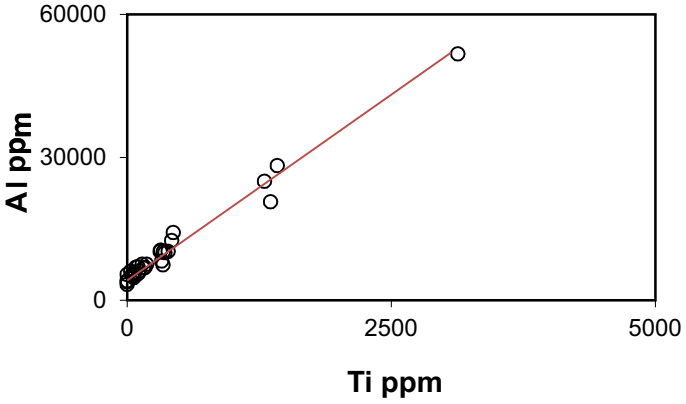
60000
30000
0
Al ppm
0
2500
5000
Ti ppm

Figure 17

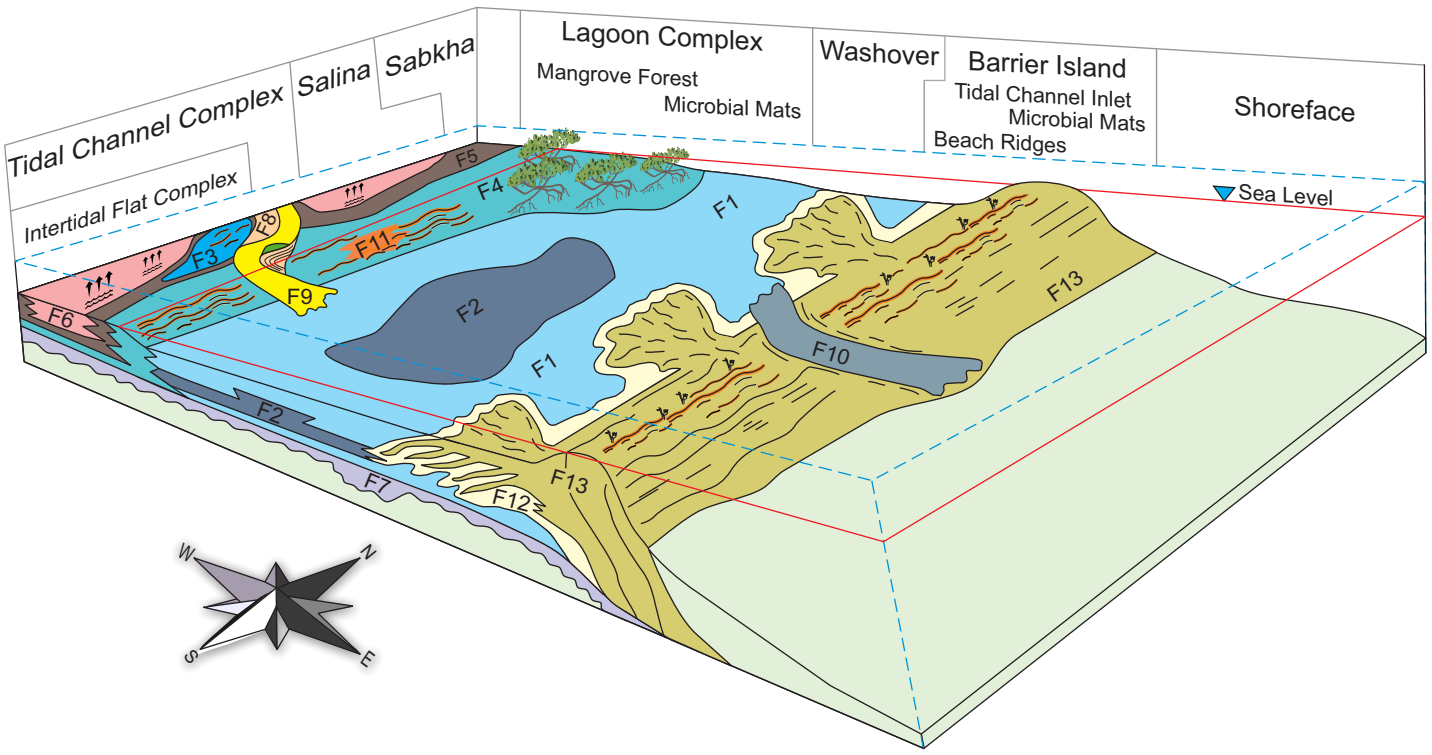
Tidal Channel Complex
Salina
Sabkha
Lagoon Complex
Mangrove Forest
Microbial Mats
Washover
Barrier Island
Tidal Channel Inlet
Microbial Mats
Beach Ridges
Shoreface
Intertidal Flat Complex
Sea Level
F1
F2
F3
F4
F5
F6
F7
F8
F9
F10
F11
F12
F13
W
N
S
E

Figure 18

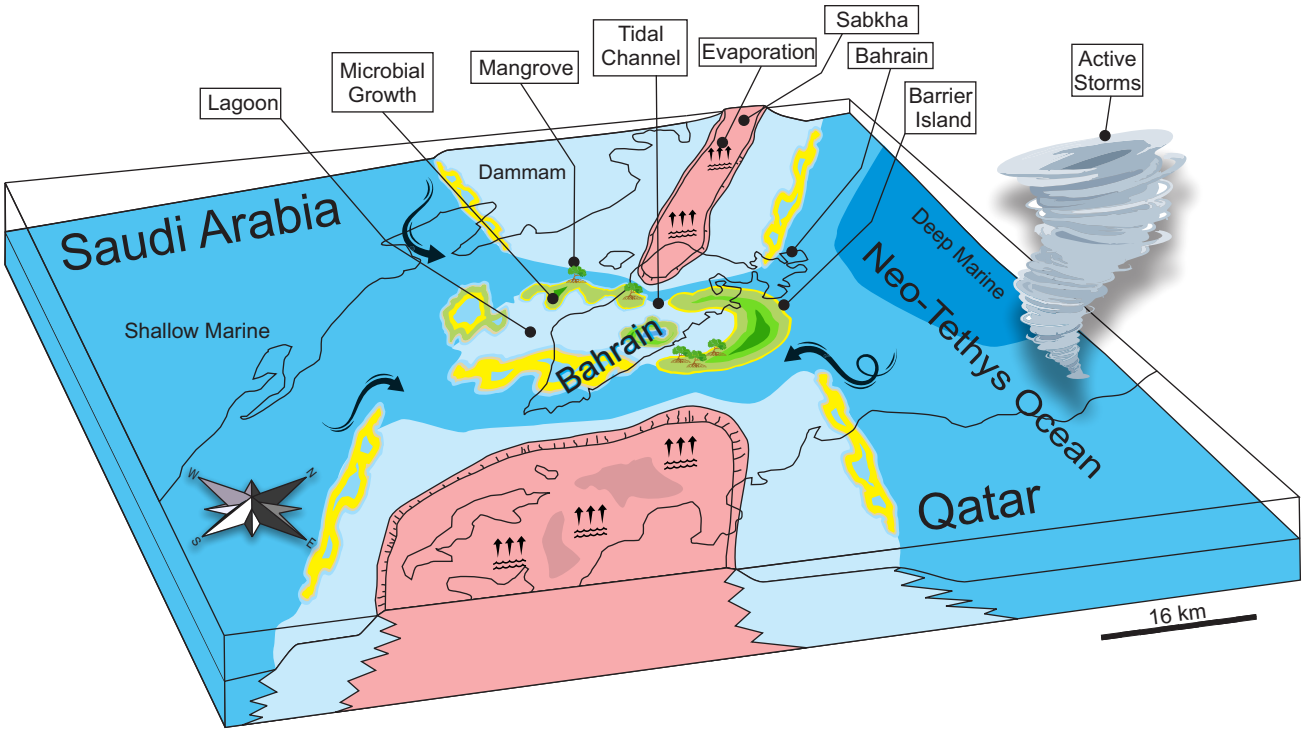
Lagoon
Microbial Growth
Mangrove
Tidal Channel
Evaporation
Sabkha
Bahrain
Barrier Island
Active Storms
Dammam
Saudi Arabia
Shallow Marine
Deep Marine
Neo-Tethys Ocean
Bahrain
Qatar
16 km

Figure 19

Facies Code	Facies Name	Facies Association Code	Facies Association	Minerals amounts (XRD)	Bioturbation	Porosity	Depositional Environment
F1	Chalky dolostone	FA-1	Lagoon Complex	100% Dolomite	Common	6%	Stressed Lagoon
F2	Lithoclastic chalky dolostone			89% Dolomite, 6% Calcite, 2.5% Quartz, 2.5% Siderite	Rare	10%	Storm Bed
F3	Peloidal dolostone			4% Quartz, 96% Dolomite	Common	11%	Lagoon Fill Deposits
F4	Foraminiferal dolostone			77% Dolomite, 18% Illite, 5% Pyrite	Moderate	3%	Restricted Lagoon
F5	Claystone	FA-2	Sabkha Complex	100% Illite	Absent	0%	Sabkha
F6	Evaporite			57% Quartz, 43% Dolomite	Absent	0%	Salina
F7	Argillaceous dolostone	FA-3	Transgressive Lag	82% Dolomite, 18% Illite	Fair to Moderate	7%	Transgressive Lag
F4	Foraminiferal dolostone			77% Dolomite, 18% Illite, 5% Pyrite	Moderate	3%	Restricted Lagoon
F8	Dolomitic marl	FA-4	Peritidal Channels Complex	75% Dolomite, 25% Illite	Absent	0%	Inland Tidal Channel Lateral Accretions/Intertidal Flat
F9	Bioturbated chalky dolostone			100% Dolomite	Common	11%	Inland Tidal Channels
F10	Cross-bedded dolostone			100% Dolomite	Common	17%	Tidal Channel Inlet
F11	Microbial dolostone			9% Quartz, 91% Dolomite	Rare	9%	Intertidal
F12	Bedded dolostone	FA-5	Barrier Island and Washover Complex	100% Dolomite	Absent	15%	Back Barrier
F13	Clinoformal dolostone			10% Quartz, 88% Dolomite, 2% Siderite	Rare	5%	Washover Barrier Island

Sample No.	Facies Abbreviation	XRD						XRF														
		Quartz	Calcite	Dolomite	Siderite	Illite	Pyrite	Na	Mg	Al	Si	P	S	Cl	K	Mn	Ti	Ca	Fe	Zn	Sr	Zr
		%	%	%	%	%	%	%	%	%	%	%	%	ppm	%	%	%	%	%	ppm	ppm	ppm
1	F1	0	0	100	0	0	0	0.617	10.59	0.5355	0.9151	0	0.05612	3586	0.032	0.0058	0.0069	20.83	0.1719	5.2	113.3	3.4
2	F1	0	0	100	0	0	0	0.994	9.498	1.05	2.785	0	0.05227	4594	0.1896	0.0080 2	0.0317 5	19.01	0.1709	12.9	116.4	10.2
3	F1	0	0	100	0	0	0	0.1359	10.28	0.7509	1.78	0	0.05103	975.9	0.0866	0.0132 3	0.0142 1	20.63	0.1504	6.2	112.9	5.6
4	F1	0	0	100	0	0	0	0.393	9.912	1.415	3.975	0.0477	0.1068	3149	0.2241	0.0141 8	0.0438 2	18.76	0.4064	9.2	89.6	14.3
5	F2	2.5	6.1	88.9	2.5	0	0	0.719	10.07	0.6097	1.621	0.0501	0.1021	4802	0.1118	0.0064 1	0.0116 2	21.84	0.1695	10	133.9	4.2
6	F3	0	0	100	0	0	0	0	11.41	0.5202	1.237	0.0936	0.06263	1154	0.0217	0.0199 7	0.0046 4	20.98	0.0636 1	8.3	98.1	1.9
7	F3	3.6	0	96.4	0	0	0	0	10.32	0.5569	1.369	0	0.07279	1320	0.0706	0.0119 6	0.0108 3	20.91	0.2286	22	145.5	7.7
8	F3	0	0	100	0	0	0	1.536	11.6	0.5351	0.8304	0.0327	0.2285	8964	0	0.0140 7	0	20.83	0.1735	7.8	160.2	2
9	F4	0	0	76.7	0	18.1	5.1	0.1387	11.02	0.8199	3.249	0.0493	0.2753	901.3	0.0437	0.0264 1	0.0328 7	20.3	0.2728	16.1	140.4	18.9
10	F4	0	0	100	0	0	0	0.24	11.54	0.6912	1.929	0.0596	0.2237	1866	0	0.0215 2	0.0086	22.01	0.1718	7.9	210	3.6
11	F4 (Mangrove Fossil)	0	0	100	0	0	0	0.227	9.629	0.6718	1.89	0.042	0.1336	1369	0.0142	0.0144	0.0156 5	23.28	0.2215	7.4	125.9	5.6
12	F5	0	0	0.0	0	100.0	0	1.068	6.47	5.169	18.24	0.0286 6	0.3767	27250	1.313	0.0032 7	0.3131	3.087	2.605	30.7	525.4	79.9
13	F5 (clast embedded)	5.2	0	68.4	0	26.4	0	0.83	7.194	2.066	6.665	0.0391 3	0.1047	8563	0.846	0.0090 2	0.1359	13.79	1.517	14.2	217.2	32.8
14	F6	56.7	0	43.3	0	0	0	0.261	2.869	0.7373	40.88	0	0.4509	4274	0.0969	0.0039 2	0.0338 7	4.493	0.4172	11.8	265.7	20.9
15	F7	0	0	81.6	0	18.4	0	0.445	8.443	2.495	7.762	0	0.04599	5040	0.7341	0.0103 6	0.1301	15.24	1.247	19.5	142.3	32.5
16	F7	0	0	100	0	0	0	0.631	10.15	1.018	2.921	0	0.051	3576	0.1255	0.0116 6	0.0311 5	19.1	0.3207	8.2	91.5	10.3
17	F7	0	0	100	0	0	0	0.0304	10.78	0.6829	1.696	0	0.05815	410.3	0.0974	0.0187 8	0.0171 8	21.12	0.0996 6	7.6	90.2	4.8
18	F7	0	0	100	0	0	0	0.047	11.23	0.3841	0.5545	0	0.0511	254.1	0	0.0164 5	0	21.64	0.0593 3	3.8	108.9	0
19	F8	0	0	75.4	0	24.6	0	1.768	8.927	2.822	8.862	0	0.07302	10810	0.6033	0.0118 8	0.1423	13.83	0.9534	18.9	110	39.2
20	F8 (bed rich in fossil fragments)	0	0	89.0	0	11.0	0	0.356	9.178	1.252	5.166	0.3371	0.2371	2930	0.0272	0.0186 5	0.0422 3	18.14	0.5449	7.6	118.9	9.3
21	F9	1.5	0	98.5	0	0	0	0	10.85	0.506	1.236	0.07916	0.05809	1200	0.0555	0.0092	0.0061 2	21.3	0.07054	6.2	125.7	2.7
22	F10	0	0	100	0	0	0	0	12.09	0.4022	0.4699	0.06223	0.06061	879.9	0	0.0182 7	0	22.28	0.06802	4.5	105.3	0
23	F10	0	0	100	0	0	0	0.0416	11.68	0.3268	0.4081	0	0.05526	281	0	0.0167 3	0	21.31	0.03441	2.9	95.7	0
24	F11	9.1	0	90.9	0	0	0	0.772	9.577	1.018	5.537	0.0315	0.08135	5033	0.3862	0.0117 4	0.0388	19.94	0.2046	10.3	116.8	10.9
25	F11	0	0	100.0	0	0	0	0	10.67	0.5489	1.494	0.08544	0.05584	1031	0.0649	0.0140 3	0.0063 8	21.21	0.1099	14.7	106.4	2.4
26	F11	8.0	0	87.9	0	0	4.1	0.789	9.987	1.014	5.103	0	0.05729	4154	0.3509	0.0089 7	0.0344 3	17.82	0.2339	8.6	107.8	8.9
27	F11	0	64.5	35.5	0	0	0	0.298	5.225	0.602	1.705	0	0.08744	2327	0.0079	0.0220 2	0.0034 5	29.69	0.161	6.3	121.7	3.1
28	F12	0	0	100	0	0	0	0.7	9.493	0.5862	1.265	0	0.0477	2999	0.0373	0.0086 1	0.0066 4	20.76	0.09573	6	113.9	4.1

29	F13	9.9	0	88.6	1.5	0	0	0.742	8.93	0.9926	4.86	0	0.06958	4064	0.4034	0.01096	0.03569	18.666	0.185	10.4	118.3	8.6
30	F13	3.3	0	96.7	0	0	0	0.336	9.198	0.6979	2.925	0	0.06414	1927	0.1129	0.01011	0.01024	20.42	0.1042	9.2	122.2	3.8
31	F13	5.4	0	94.6	0	0	0	0.593	9.142	0.7536	3.631	0	0.05588	3455	0.2215	0.0091	0.01859	19.84	0.1098	6.9	113.3	6.5
32	Geode Crystals	0	88.7	11.3	0	0	0	0	1.93	0.4703	0.866	0	0.06664	606.7	0	0.01355	0.00639	35.02	0.07526	5.3	150.5	5.4